8

Lessons from Shoemaker–Levy 9 about Jupiter and Planetary Impacts

Joseph Harrington
Cornell University

Imke de Pater
University of California, Berkeley

Stephen H. Brecht
Bay Area Research Corporation

Drake Deming
NASA Goddard Space Flight Center

Victoria Meadows
Jet Propulsion Laboratory, California Institute of Technology

Kevin Zahnle
NASA Ames Research Center

Philip D. Nicholson
Cornell University

*Dedicated to the memory of Eugene Merle Shoemaker (1928–1997)*

8.1 INTRODUCTION

From July 16 through 22, 1994, at least 16 fragments of comet Shoemaker–Levy 9 hit Jupiter. The events caught worldwide public attention, which was heightened by several factors. The impact sites were visible in small telescopes, and many people took their first magnified look at the night sky. Also, the public was becoming aware of the terrestrial impact hazard from near-Earth objects, the optics of the Hubble Space Telescope (HST) had been corrected the previous December, and the World Wide Web was bringing the Internet into the homes of ordinary citizens. This chapter reviews our current understanding of these landmark events.

Impactors as large as Shoemaker–Levy 9 (hereafter SL9, and also D/1993 F2) currently hit Jupiter every few centuries (Bottke *et al.* 2002, Levison *et al.* 2000, Roulston and Ahrens 1997, Zahnle *et al.* 2003, Chapter 18), but they were much more frequent during planetary accretion. If all of Jupiter's heavy elements were delivered by SL9-like impactors, the average rate over its existence would be one impact every 20 minutes. Impacts 10^5 times less energetic than SL9 occur annually on Earth, and they involve similar physics (Figure 8.1 and Boslough and Crawford 1997,

Boslough and Gladstone 1997, Shuvalov 1999). SL9 offered us a rare glimpse of this process, and also provided a perturbation experiment of the sort that is very difficult to arrange in planetary science.

This chapter emphasizes results about Jupiter and impact processes that extend beyond SL9. The next section presents a brief review of impact circumstances, categories of observations, the major sources in the literature, and points of historical reference. We then review the atmospheric physics of a typical large event and a phased modeling framework. Each phase's discussion includes observations and physical models. The puzzle of the expanding rings seen by HST closes the section. Next we present results on atmospheric chemistry and dust, the state of modeling their creation and dissipation, and the implications for the "normal" state of Jupiter's atmosphere. Observations and models of the magnetosphere and its coupling to the atmosphere complete our review. We conclude with a summary and suggestions for future work.
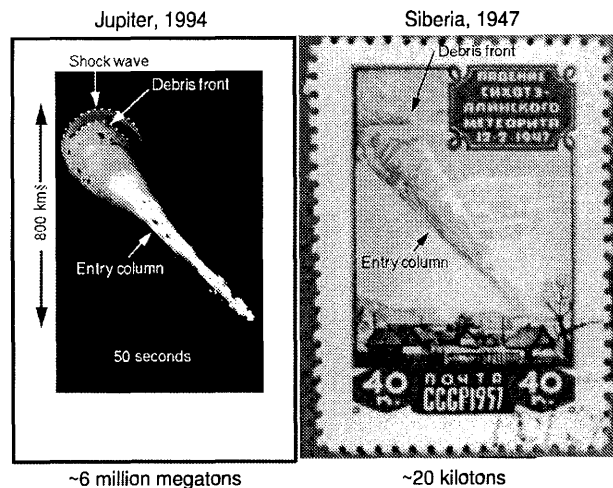
Figure 8.1. Atmospheric impact physics over many orders of magnitude. Left: Model of SL9 plume by the Sandia group. Colors correspond to temperature. Note the extended entry/ejection column. Right: Eyewitness painting of 1947 Sikhote-Alin impact in Siberia by P. I. Medvedev. After Boslough and Crawford (1997), copyright © 1997 New York Academy of Sciences, U.S.A. At the time of going to press a colour version of this figure was available for download from http://www.cambridge.org/9780521035453.

Figure 8.2. Top: SL9 discovery image. Courtesy C. Shoemaker and D. Levy. Bottom: HST image of SL9 before impact. Courtesy H. Weaver and T. E. Smith (STScI) and NASA. At the time of going to press a colour version of this figure was available for download from http://www.cambridge.org/9780521035453.

8.2 IMPACT CIRCUMSTANCES

Jupiter most likely captured SL9 in 1929 ± 9, and tidally disrupted it during a perijove passage just 0.3 Jupiter radii above the cloudtops on July 7, 1992 (Chodas and Yeomans 1996, see also Chapter 12). Carolyn S. Shoemaker discovered SL9 on March 24, 1993, on a photographic plate that she, Eugene M. Shoemaker, and David H. Levy took with the Palomar 0.46-m Schmidt telescope (Shoemaker *et al.* 1993, Figure 8.2). On May 22, 1993, Nakano *et al.* (1993) predicted the impacts.

Asphaug and Benz (1994, 1996), Scotti and Melosh (1993), and Solem (1994, 1995) all derived the mass and density of the parent comet from tidal breakup models. The models required strengthless, slow rotators with diameter 1.5–2 km and density 0.5–0.6 $g cm^{-3}$ (mass $\sim 10^{15}$ g) to match the number of fragments and the chain length observed over time. No SL9 model required impactors inconsistent with these estimates. The images and orbit suggested to Melosh and Schenk (1993) that crater chains on Galilean satellites were caused by impacts of tidally-disrupted, Jupiter-orbiting comets. Similar tidal splitting near Saturn is unlikely since the periapse distance required is below the planet's surface (Asphaug and Benz 1996).

The fragments (Figure 8.2) were named in impact order, A first and omitting I, O, X, Y, and Z. Fragments P and Q split after being named, begetting P2, P1, Q2, and Q1 in impact order. Fragments F, J, P2, P1, and T disappeared before impact and no impact phenomena were reported for them. Impact velocities were 61.12–61.68 km s^{-1} relative to System III rotation (λ_{III}), the interior/magnetic field rotation rate. Incidence angles were 42.49°–43.30° from vertical, azimuth angles were 13.34°–18.57° west of north, planetocentric latitudes were 43.22°–45.02° south (47.06°–48.85° planetographic). Chodas and Yeomans (1996) and Nicholson (1996) tabulate these values along with fragment
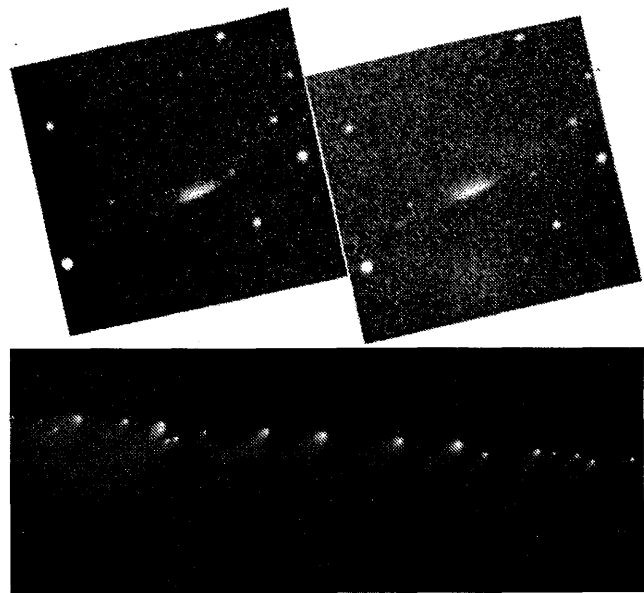
orbital elements, impact times, longitude, observed phenomena, references, etc.

Because the impacts occurred 3.4°–8.8° behind the dawn limb (Chodas and Yeomans 1996), the *Galileo* spacecraft, en route to Jupiter, acquired the only direct view (Carlson *et al.* 1995, 1997, Chapman 1996), which occurred just behind the rising limb as seen from Earth. The Extreme Ultraviolet Explorer, International Ultraviolet Explorer, ROSAT, *Ulysses*, and *Voyager 2* spacecraft also attempted observations (see Section 8.5).

Nearly all of humanity's telescopes observed the impacts and aftermath (Figure 8.3). The NASA Infrared Telescope Facility (IRTF) dedicated over one month of telescope time (Orton *et al.* 1995) and HST devoted about 140 orbits (Clarke *et al.* 1995, Hammel *et al.* 1995, hereafter HAM95, McGrath *et al.* 1995, Noll *et al.* 1995, Prangé *et al.* 1995, Weaver *et al.* 1995, West *et al.* 1995). The events were among the first observations for many instruments, including the Wide-Field and Planetary Camera 2 (WFPC2) on HST (which corrected the primary mirror's aberrations), MIRAC2 at the IRTF (which had one of the first 128 × 128 arrays sensitive in the 5–30 μm range), and the multiple-instrument mount at the IRTF. There were no 8-meter optical/IR telescopes at the time and the lone 10-meter telescope (Keck I) had just seen first light.

SL9 represented the first broad use of the Internet for communicating results or coordinating an effort within the astronomy community. This was facilitated in particular by a server at the University of Maryland. High-end workstations ran at 40 MHz and a very large disk held 2 GB. The supercomputers used for the early models provided only ~ 1 Gflops, which limited most computations to 2 spatial dimensions (2D) and only ~ 100 zones of resolution, and also restricted the number of cases an investigator could run.

There are over 300 refereed papers on SL9, which precludes exhaustive references here. Many appeared in special issues or sections of *Science* (March 3, 1995), *Icarus* (June
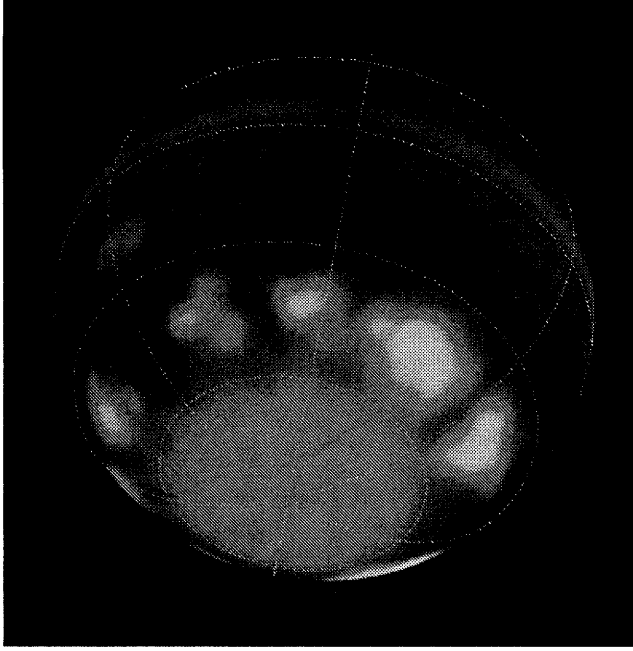
Figure 8.3. Remapped composite of impact site images taken at 2.3 μm at the Palomar 5-meter telescope. In this strong CH$_4$ band, stratospheric aerosols deposited by the impacts stand out against the dark troposphere. Note also the high-altitude hazes above the south pole and the Great Red Spot. At the time of going to press a colour version of this figure was available for download from http://www.cambridge.org/9780521035453.

1996), and *Geophys. Res. Lett.* (June 1, 1994; June 15, July 1 and September 1, 1995). Refereed proceedings came from conferences in Baltimore in 1995 (Noll *et al.* 1996), Munich in 1995 (West and Böhnhardt 1995), and Paris in 1996 (*Planet. and Space Sci.*, October 1997).

8.3 ATMOSPHERIC PHYSICS

The large impact events followed a consistent chronology and morphology, whereas smaller impacts had reduced or truncated effects (Nicholson 1996, HAM95). We next summarize this sequence of events to introduce the accepted SL9 terminology, referring as needed to figures out of order. Then we divide a nominal event into five phases that have been used for modeling. Our discussion of the atmospheric physics of each phase follows.

The light curves tell much of the story. A fragment's coma emitted the *first precursor* upon impact with the atmosphere as a meteor shower near the limb (Figure 8.4, #1–3). The fragment penetrated into the atmosphere, disrupting and vaporizing as it fell. A *plume* (Figure 8.1) consisting of the shock-heated gas, the vaporized fragment, and entrained air rose back up the entry path and blew out of the atmosphere. The plume's early thermal emission caused the *second precursor* (Figure 8.4, #8) and reentry of fast material on horizontal trajectories caused the *third precursor* (Figure 8.9, PC3). A few fragments had large enough comae that the precursors were superposed on a rising *leader emission* (Figure 8.4, #1 & 3) from the entering material. Compression of the atmosphere upon plume reentry caused the *main event* (Figure 8.9, ME), which outshone the planet at many wavelengths. At the end of plume reentry (1000 s after impact) there was a *flare* (Figure 8.9, F) at wavelengths near 0.9 μm

Table 8.1. SL9 Event Phases

Phase	Duration	Scale (km)	Velocity (km s^{-1})	Temperature (K)
Impact	5 seconds	few×100	60	100–40 000+
Blowout	few×10 min	few×100	60	100–40 000
Plume flight	20 min	20 000	12	8000–10
Plume splash	few hours	20 000	12	100–3500
Dissipation	10–300 years	global	0.2	~100

After Harrington and Deming (2001).

that briefly outshone the main event. The falling light levels *bounced* (Figure 8.9, B & 2B) several times with a 10-minute period. All of these events occurred within about 30 minutes of impact.

Subsequent imaging by HST showed a *streak* of material (Figure 8.6, S) encircling the impact location and extending to the southeast (the direction from which the fragments arrived and toward which the plumes flew). One or two expanding, narrow *HST Rings* (Figure 8.6, R1 & R2) propagated through the streak and into a broad *crescent* (Figure 8.6, C) of scattered material as far as 13 000 km from the *impact sites* (Figure 8.6, +). *McGregor's ring* (Figure 8.10), an off-center thermal emission effect, encircled all the above features and expanded for several hours after impact. Zonal winds smeared the impact sites in longitude within a few days, and the particulates spread in latitude and disappeared over several years.

Computational limitations made SL9 models challenging. Harrington and Deming (2001) extended an approach of earlier modelers by defining five independent modeling phases (Table 8.1). By using the output of one phase's model as input to the next, one preserves the physics reasonably well while maintaining computational tractability. This approach enables the testing of models of early phases that have few observations, because one can compare their influences on later, well-observed phases. Note that there is sometimes considerable temporal (but not spatial) overlap between successive phases. We discuss the observations and models of each phase below, and end the section with a discussion of the enigmatic HST rings.

8.3.1 Impact

Data from the impact phase are limited. The first precursor brightening seen by Earth-based observers lasted up to 90 s (Figure 8.4, #1–3, and Figure 8.5, top A panel). Spectra of the first precursors for C, G, and K and leader emission for G and K all show increased continuum emission with no appreciable emission or absorption features (Dinelli *et al.* 1997, Knacke *et al.* 1997, Meadows and Crisp 1995). Meadows *et al.* (2001) model this as a very high altitude, thermally emitting source seen through a short path length of atmosphere, which was probably coma dust falling close to the limb as a meteor shower. About 40 s after the initial brightening, and a few seconds past its peak, *Galileo* saw a bright, unresolved flash at the impact site (Chapman 1996, Figure 8.4, #6). This was the entering fragment.

A comet fragment disrupts as it falls, vaporizing entirely and depositing most of its kinetic energy near its terminal atmospheric depth. Carlson *et al.* (1997), Crawford *et al.* (1994), and Zahnle and Mac Low (1994) calculated

peak temperatures of 30 000–40 000 K. Mac Low and Zahnle (1994) estimated the required modeling grid scale at ∼10 meters, tiny compared to the few hundred kilometers the fragment travels. The time span is also large compared to the required time step. Given the state of computation outlined above, all models of this phase had to compromise either resolution, number of dimensions, or important physics.

Three groups published gridded two-dimensional (2D) numerical models. All adjusted the atmospheric profile to compensate for the 45° inclination of the impact vector and used cylindrical symmetry about the channel axis. The Sandia group (Boslough *et al.* 1995, Boslough and Crawford 1997, Crawford 1996, Crawford *et al.* 1994) used their laboratory's CTH and PCTH codes. Mac Low (1996), Mac Low and Zahnle (1994), Zahnle and Mac Low (1994, 1995), and Zahnle (1996) used ZEUS. Shoemaker *et al.* (1995) used MAZ, but the model was not fully developed at the time of Dr. Shoemaker's death. CTH and MAZ were developed to model nuclear explosions, while ZEUS was developed to model astrophysical fluid dynamics, so they are all appropriate for modeling the physical conditions of the impacts. The smoothed-particle hydrodynamics (SPH) model of Ahrens *et al.* (1994a,b), Takata *et al.* (1994), and Takata and Ahrens (1997) is unique among those mentioned here because it handles both the impact and blowout phases in a single, 3D model.

All impact models predicted hot gas traveling back up the heated entry channel, but they differed by many scale heights ($H \sim 25$ km) in their predictions of a fragment's terminal depth. For an impactor 1 km in diameter, the Sandia group predicted detonation at ∼125 km below the 1-bar level and Zahnle and Mac Low (1994) predicted peak energy deposition 50–100 km below 1 bar. However, the SPH model predicted continuous deposition 100–300 km below 1 bar.

Zahnle and Mac Low (1994) questioned whether the SPH model could resolve the instabilities responsible for breaking up a fragment. Takata and Ahrens (1997) addressed these concerns insufficiently, in our view, by presenting additional models that did not meet the resolution criteria of Zahnle and Mac Low (1994). However, they also pointed out the shortcomings of 2D models. Roulston and Ahrens (1997) model a viscous fluid that breaks up by both Rayleigh–Taylor and Kelvin–Helmholtz (KH) instabilities. However, they use a non-standard expression for the growth rate of KH instabilities. Their fluid model roughly reproduces all three gridded models' results when run with their respective resolutions and impactor sizes. They conclude that a 1-km fragment delivers most of its energy near 50–100 km below 1 bar, that models require ∼25 grid cells across the impactor radius to achieve convergent results, and that the 8-element resolution of Takata *et al.* (1994) was insufficient. Well-resolved 2D and 3D Venus impact modeling (Korycansky *et al.* 2000, 2002) shows that 2D models with slightly differing initial conditions follow more divergent evolutions than 3D models. The qualitative results are not dramatically different, however.

Phenomenological terrestrial bolide models extrapolated up to the SL9 scale predict a much higher break-up due to early and frequent fragmentation. It is uncertain how well such models translate to objects 10^9 times as massive and moving several times faster in a different atmosphere. The 1-km case of Borovička and Spurný (1996) explodes 72
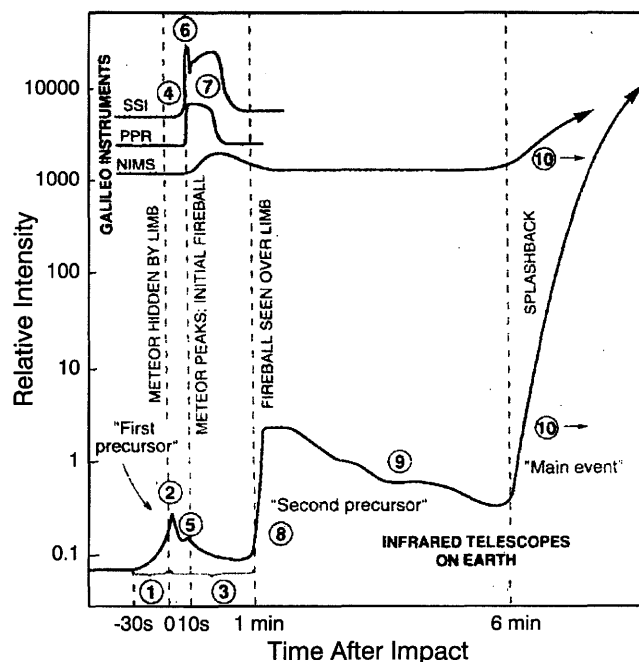
Figure 8.4. Schematic of the early light curves. 1–3: coma meteor shower (also called leader emission), 4 & 6: bolide entry, 5: possible reflection of bolide emission on trailing coma dust, 7: fireball, 8: plume becoming visible over limb, 9: cooling plume, 10: plume reentry. Adapted from Chapman (1996).

km above the 1-bar level. The *Galileo* observations indicate deeper penetration (Borovička and Spurný 1996).

8.3.2 Entry Response/Blowout

The entry response phase differs from the impact phase mainly in the need to model a larger spatial scale, and from the plume splash phase by the need to resolve smaller and faster effects. In this phase, the atmosphere responds to the new energy, momentum, and material it received from the fragment. A shock propagates away from the entry channel in all directions. Superheated comet material and entrained air (the *fireball*, Figure 8.4, #7) travel back up the entry channel (Figure 8.1) at speeds exceeding $10\,\mathrm{km\,s^{-1}}$. This plume traverses the atmosphere, and the resulting ionospheric perturbation in turn disturbs the magnetosphere (Section 8.5). The surrounding atmosphere continues to adjust to these events. Shock physics and non-hydrostatic hydrodynamics dominate. The four impact modelers continued in this phase with their respective codes. Sandia and Shoemaker switched to 3D and reoriented the entry channel to 45°. The SPH group continued with the same computational grid as before, while the others all decreased their resolutions.

Since the impact sites were not yet in view from Earth, the only observations of this phase were the *Galileo* light curves (Figure 8.4, #7). The HST rings may have originated in this phase or in response to the landing plumes, but they were only seen much later (Section 8.3.6).

Detection of seismic waves was a great pre-impact hope (Deming 1994, Gough 1994, Hunten *et al.* 1994, Kanamori 1993, Lognonné *et al.* 1994, Marley 1994). Their refraction
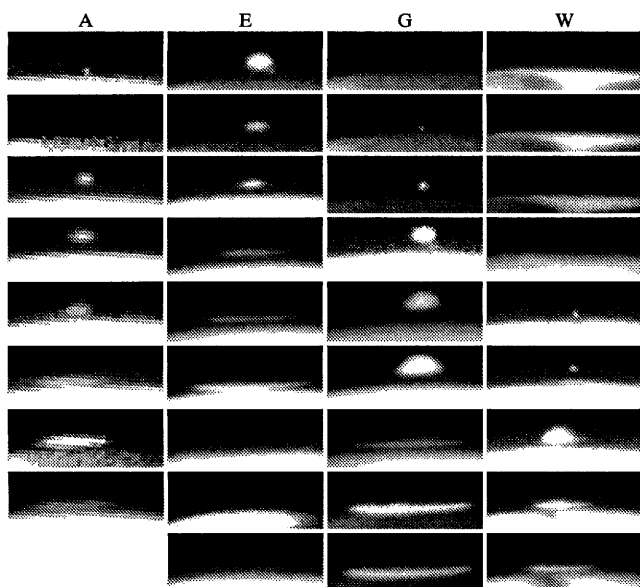
Figure 8.5. HST images of plumes from the A, E, G, and W events, seen on Jupiter's limb. The plumes continued to slide after they had fully collapsed. Note emission from the hot ejection tube in the first E and fourth G images. Adapted from Harrington and Deming (2001), after original presentation by HAM95.

through the interior and their reflection from the putative molecular–metallic hydrogen boundary would have given the first direct measurements of the depth and abruptness of that transition, as well as the density profile of the upper interior. Unfortunately, nothing was seen for any event, including L, the largest. Walter et al. (1996) and Galdemard et al. (1997) derived upper limits for impact energy of 1.5–2×10^{28} erg from the non-detections. The total mass estimated above yields 2×10^{28} erg, and Nicholson (1996) estimated that fragment L carried 40% of the mass. The limit thus indicates that the parent comet was not much bigger than found by the tidal break-up models cited above.

All entry–response models produced ballistic plumes (see next section), and most explored the question of plume heights. Preferring deep explosions, Crawford (1996) showed models where entrained, presumably reflecting, cloud material from different-sized impacts reached the same height (1500–2000 km) even though additional, presumably clear, material rose to different (and greater) heights. Zahnle (1996) countered that smaller impactors exploded higher, spread their energy over a smaller mass of air, and had to move less air to get to space. Zahnle's semi-analytic model closely follows lines of constant plume height for the size range of the SL9 impactors, but diverges for larger or much smaller impactors. Without a physical model for the mechanism by which the plumes became visible (presumably sunlight scattered by dust, but how much dust and where generated?), it is difficult to evaluate the various models based on the observed plume heights. This avenue is worth further study.

8.3.3   Plume Flight/Landing

Visible material in the plumes rose 2300–3100 km above the cloudtops (Jessup et al. 2000), the latter corresponding to

a ~12 km s^{-1} vertical ejection velocity component. Figure 8.5 presents the HST images of plumes from the A, E, G, and W events (HAM95). Initially, the plumes were so hot they emitted in the visible: the *Galileo* Photopolarimeter Radiometer and Ultraviolet Spectrometer both measured emission at 8000 K (Carlson et al. 1997). Their appearance above the limb produced the second precursors in the ground-based light curves (Boslough et al. 1995, Nicholson 1996, and Figure 8.4, #8).

Dinelli et al. (1997), Knacke et al. (1997), and Meadows et al. (2001, 2004) obtained time-resolved near-IR spectra for several of the second precursors. These indicate a continuum source (presumably dust in the plume) transmitting through a long path length of atmospheric CH_4, which produces strong absorption features centered around 2.3 μm. The depth of CH_4 absorption decreased with time, vanishing near second-precursor peak brightness, 2–3 minutes after impact, when the plume had cleared the limb. Color temperatures from the 2.0–2.4 μm data were first reliable at this time. For the K plume, the continuum color temperature had dropped to 700 K by 3.2 minutes after impact and to 400 K by 8 minutes after impact (Meadows et al. 2004). These temperatures are consistent with 370 K silicate dust reported by Nicholson et al. (1995a) at 8 minutes after the R impact. At 3.5 minutes CH_4 appears in emission at 2.3–2.4 μm. Dinelli et al. (1997) obtained a 3.53–3.545 μm spectrum of the C second precursor between 1.7 and 3 minutes after impact. They observed hot CH_4 emission with a derived temperature of 2000–5000 K. These spatially unresolved measurements are dominated by the hottest material in the plume, but most plume gas quickly cools by adiabatic expansion to tens of K as the plume's radius increases from a few km to over 6000 km.

All entry–response models ran through at least the beginning of plume flight, but none published the inputs needed for optimal modeling of the plume splash. Shoemaker et al. (1995) indicated a maximum plume flight time of only 10 minutes, but the observations show otherwise. The Sandia group's model stopped short of presenting the atmospheric reentry boundary conditions or detailed impact-site images. However, these codes can model the hydrodynamics relevant in the early part of this phase, which ballistic models (below) cannot. For example, while much material left the computational grid of Zahnle and Mac Low's longest-running model, the model produced some features that may be relevant to the expanding rings seen by HST (Section 8.3.6), and also the only published plume velocity distributions.

Harrington and Deming (2001), Pankine and Ingersoll (1999), and Zahnle and Mac Low (1995) all simplified the physics to ballistics to explore the parameter space of flying plumes. Pressure gradients drop as the inverse fourth power of time, so gradients in the young plumes far exceeded those encountered later in flight. The initial expansion impulse thus dominates subsequent ones except those acting over long intervals. The only consistent force is gravity, so models initialized with velocity and evolving only under gravity are appropriate.
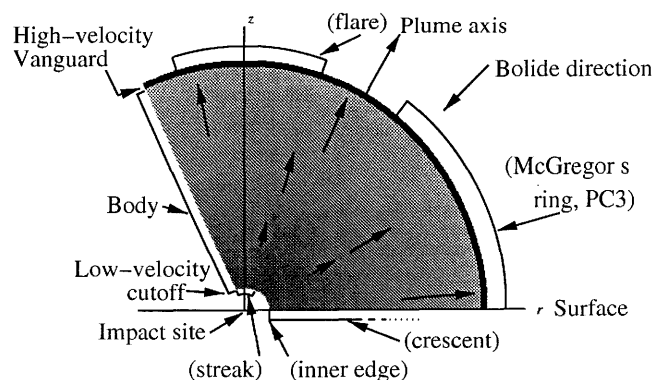
Zahnle and Mac Low (1995) used a vertical 2D ballistic plume to show that the main event was caused by plume infall (see next section). Pankine and Ingersoll (1999) explained the varying impact-pattern rotations by parametric
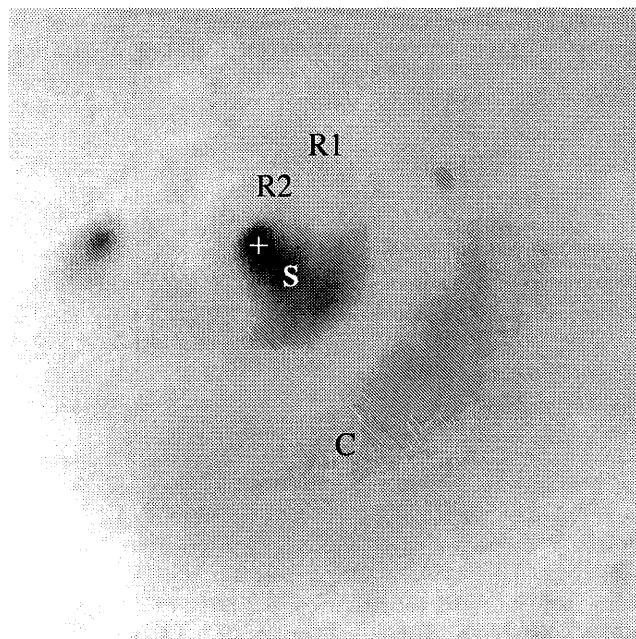
Figure 8.6. The G impact site, orthographic projection. Suspended material is dark in this HST image. The impact site is marked "+", and is at the center of the complete (and expanding) rings (marked "R1" and "R2"), just inside the northwest portion of the streak region (marked "S"). The inner edge of the crescent (marked "C") slid less near the axis of symmetry than away from it, whereas the outer edge slid more near the axis. The tiny D event streak is on the left.


Figure 8.7. Schematic cross section of a plume after it leaves the atmosphere. This side view shows a plume's principal parts, the surface effects to which they give rise, and the mass–velocity distribution. "Body" refers to plume mass that is slower than the maximum velocity. Other terms are defined in the text. Mass rises up into a cone from the impact site, which is located at its (downward-pointing) apex. Vectors in the plume body indicate *initial* velocities. Hydrodynamic models (Figure 8.1) show that plume density has angular as well as radial dependence. The entry column shown in Figure 8.1 would extend below and to the left of this figure. After Harrington and Deming (2001).

simulation of plume material sliding under Coriolis influence after landing on the atmosphere. Harrington and Deming (2001) calculated the boundary conditions for the plume splash. Harrington and Deming (2001), Pankine and Ingersoll (1999), the Sandia group, and the SPH group all calculated synthetic impact-site views. The plumes slid across the atmosphere after landing (Figure 8.5), and models that do not take this into account (Sandia, SPH, and certain cases of Harrington and Deming 2001) show impact-site images with material connecting the streak and crescent regions. The data (Figure 8.6) show no connecting material. Harrington and Deming (2001) and Pankine and Ingersoll (1999) varied parameters in their Monte Carlo velocity distributions and their mechanistic sliding schemes to produce images that better match the data.

Harrington and Deming (2001, Figures 8.7 and 8.8) mapped the streak to material that flew vertically and thus could not slide far upon landing, the inner crescent edge to the speed ($\sim$5 km s^{-1}) at which reentry could produce carbonaceous grains, and the outer crescent edge to a sharp decrease in the projected mass–velocity distribution. They also propose a narrow *vanguard* of higher density at the maximum plume velocity. This feature explains the third precursors and flare in the light curves (Figure 8.9) and McGregor's ring (Figure 8.10). Using time- and location-dependent infall fluxes from this model, the Deming and Harrington (2001) atmosphere model produces all three features. The vanguard appears in the derivative of the cumulative plume velocity distribution published by Zahnle *et al.* (1995), which they explain by calling upon a 1-D analytic solution of Zel'dovich

and Raizer (1967). Only some of their models follow this distribution. In 3D hydrodynamics, such structures tend not to be stable, so work is needed to determine whether the instability timescale is short compared to the plume flight time. However, the vanguard explains the data very well, so models without one must propose other mechanisms that produce the third precursor, the flare, and McGregor's ring. A leading density enhancement could increase a terrestrial plume's efficiency at producing devastation, reducing the minimum impactor size that would cause a given level of damage.

8.3.4   Plume Splash

The plume splash phase covers the atmosphere's reaction to the infalling plume, which is both physical and chemical (Section 8.4). Particulate grains formed following the ejection shock (Friedson 1998) and ablated during reentry (Moses 1997). Subsequently, the grains advected with the gas and fell under gravity. After falling into the stationary atmosphere, they ceased their horizontal motion but continued to fall. When they reached the stratosphere, their terminal velocities were very slow, leaving the striking, quasi-static patterns (HAM95) that have become the hallmark of the SL9 impacts (Figure 8.6). The grains' exact composition is uncertain (West *et al.* 1995), but their size distribution extended below 1 μm (Pryor *et al.* 1997, West 1995). The material is bright in CH$_4$ bands, indicating deposition altitudes at least as high as a few mbar (Molina *et al.* 1997). The streaks had optical depths exceeding unity (Sanchez-Lavega *et al.* 1998), and even the crescents contained significant particle column densities. The inner crescent edges were $\sim$6000 km from the impact site. The largest events showed dense rays in their crescents that pointed to a location 1000–2000 km southeast of the impact sites. These may have been due
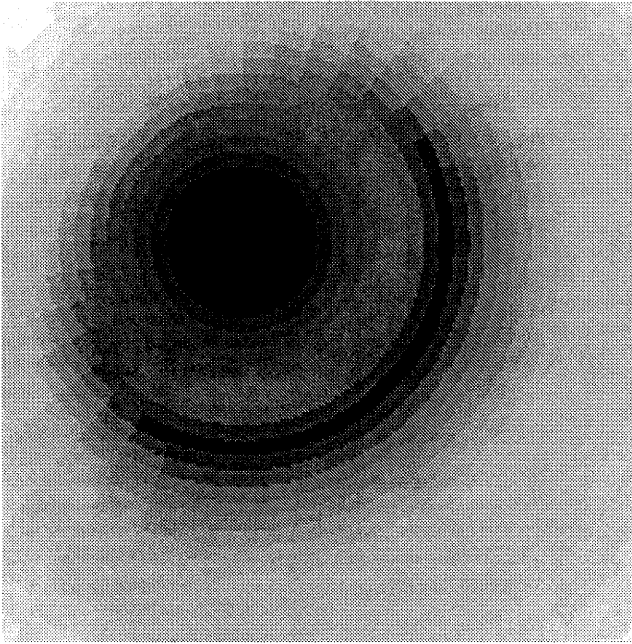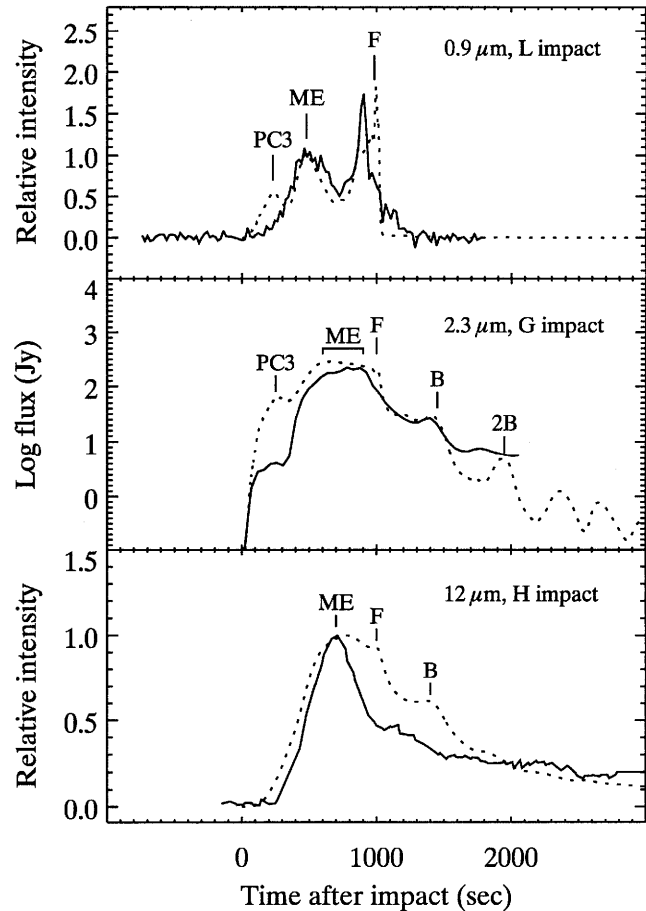
Figure 8.8. Nominal impact-site model of Harrington and Deming (2001). Intensity is proportional to gas mass deposited. The formation and redistribution of dark grains is still poorly understood, so feature locations are more important than relative intensities. The inner crescent edge has slid 6000 km from the impact site. Figure width is 24 000 km, similar to Figure 8.6. The model produces McGregor's ring but it is well outside the image.

Figure 8.9. Observed and model main event light curves. Solid lines show data from Schleicher *et al.* (1994, L event), McGregor *et al.* (1996, G event), and Lagage *et al.* (1995, H event). Dotted lines show synthetic light curves at these wavelengths from a single model by Deming and Harrington (2001). The model used plume infall fluxes from the nominal case of Harrington and Deming (2001) with sliding turned off, and was not adjusted to match the observations. The third precursor (PC3), main event (ME), flare (F), and bounces (B, 2B) are as indicated. The cylindrical model has a 2D pie-slice geometry with the apex at the impact site. In a 3D model, bounces in different pie slices would destructively interfere to reduce the bounce light-curve amplitude. The flare and third precursor are due to the vanguard feature of the plume model. Adapted from Deming and Harrington (2001).

to Rayleigh-Taylor instabilities in the pre-ballistic plumes (HAM95).

HAM95 observed plume material sliding on the atmosphere (Figure 8.5). The crescent locations and plume heights corroborated this interpretation. The G event plume rose to ~3100 km (Jessup *et al.* 2000), but the outer crescent edge is ~13 000 km from the impact site, more than twice as far as a ballistic object can fly under gravity given this maximum height and assuming no bias in plume speed with ejection direction. The symmetry axis that split the crescent and contained the impact site was rotated 14°–21° from the surface track of the incoming fragment. Pankine and Ingersoll (1999) and Jessup *et al.* (2000) model the rotation as a Coriolis effect during plume flight and sliding. Sliding occurs because the tangential velocity component is conserved across the reentry shock.

McGregor *et al.* (1996) reported emitting rings that encircled all other impact phenomena after the G and K impacts (Figure 8.10). The ring centers were displaced to the southeast of the impact sites, and they had expanded 14 000 and 18 000 km in that direction by 4700 and 7400 s after impact, respectively. The implied 1.5 km s^{-1} speed exceeds the sound speed on Jupiter. McGregor *et al.* suggested they were due to material sliding across the atmosphere, and the spectral energy distribution of the ring emission prompted Wilson and Sagan (1997) to suggest that tholins produced by shock chemistry were responsible. Although only one team reported this effect, the detection is unambiguous, appearing in several images for each of several events at several wavelengths in the 3–4 μm band.

Deming and Harrington (2001) studied the plume

splash using the Zeus3D hydrodynamics code, to which they added gray radiative transfer and grain advection. The model calculates flow fields and light curves, and can potentially calculate spectra. To produce the plume mass and momentum infall fluxes that drive this model, Harrington and Deming tuned their ballistic plume model to match the HST impact-site images (Figure 8.8). That model had a simple geometry with three free parameters (plume tilt, azimuth, opening angle) and a selection of sliding mechanisms (one parameter). Constraints on ejection speed and minimum velocity came from the observations directly. The parameters had mostly independent effects on the images and equaled the number of measurable effects in the data. The driving fluxes for the atmosphere model came from a ballistic plume with the fitted parameters but no sliding (since the atmosphere model does that realistically). There are minimal free
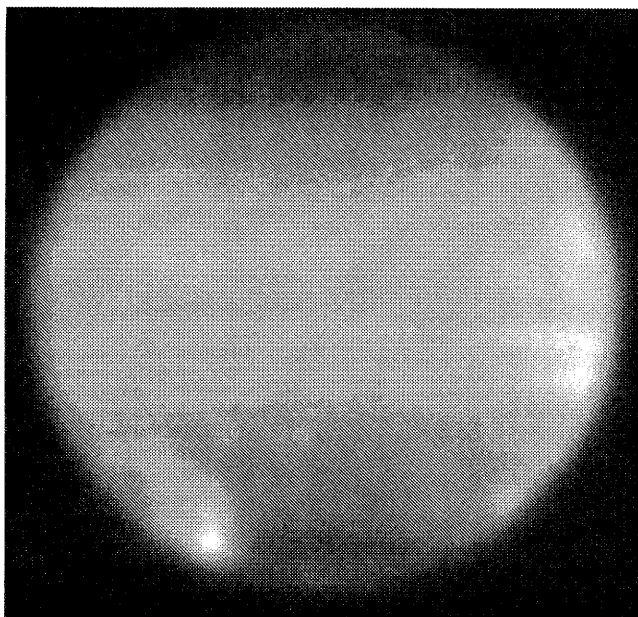
Figure 8.10. McGregor's ring for the K event, 3.08 μm. The ring is more complete and much larger than the crescent feature observed by HST. Here, at 78 minutes after impact, the radius is 14 000 km. Two hours after impact the radius was 18 000 km. After McGregor *et al.* (1996).

parameters in the atmosphere model. Synthetic light curves match the diverse observations well over their 0.9–12 μm range (Figure 8.9), even though the light curves come from different events.

Deming and Harrington find that the immediate re-entry of horizontally-ejected, fast plume material (part of the vanguard) drives a lateral shock (Figure 8.11) that produces the third precursor and McGregor's ring. The plume re-compressed on landing, and the resulting conversion of kinetic to thermal energy gave rise to the main event (Graham *et al.* 1995, Nicholson 1996, Zahnle and Mac Low 1995, Zahnle 1996). Radiating shocks traveled up through the infalling plume material and down into the atmosphere. (Melosh *et al.* 1990) concluded that the Cretaceous–Tertiary impact plume similarly heated the Earth's atmosphere, lighting global wildfires.

The Deming and Harrington model identifies the flare at 1000 s after impact (Schleicher *et al.* 1994, Fitzsimmons *et al.* 1996a, Ortiz *et al.* 1997) with the near-simultaneous arrival of the vertically launched portion of the vanguard. Observations of hot CO (Meadows and Crisp 1995) are coincident with the flare and are consistent with the model's peak temperature of 2500 K (but see discussion in Section 8.4.1). Radiative time constants for Jupiter's stratosphere are usually weeks or months (Bézard 1997), but the main event lasted only 20 minutes. Three effects are at play: a fast horizontal expansion, increased radiation at higher temperature, and the plume's delivery of more effective IR radiators (CH_4, H_2O, CO, silicate dust). Deming and Harrington show that of the first two effects, expansion is more important.

The first of the 10-minute bounces (Nicholson *et al.* 1995b) may come from new air rushing in to fill the void left by the collapsing plume. Later bounces come from an atmospheric oscillation at the acoustic cut-off frequency. Thus,
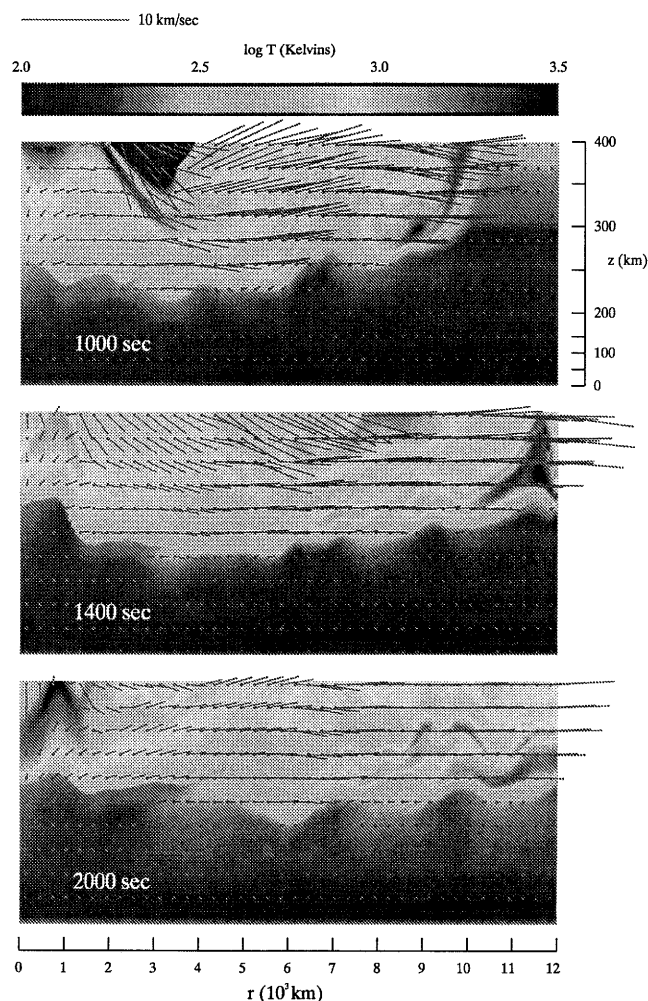
Figure 8.11. Atmospheric plume landing response model. Color is temperature and anchored streamers show flow. The McGregor's ring shock is leaving the right edge of the grid, while the vanguard makes its final re-entry near the origin in the 1000 s panel. $z = 0$ is 1 bar pressure. Reprinted from Deming and Harrington (2001). At the time of going to press a colour version of this figure was available for download from http://www.cambridge.org/9780521035453.

although seismic waves returning from the interior were not strong enough to be detected, seismic waves returning from the lower atmosphere apparently were.

The model's McGregor's ring shock is sufficiently hot to produce thermal emission at the 3.08–3.59 μm observation wavelengths, but not hot enough to be visible at shorter wavelengths, even in other CH_4 bands. Since no other observers used these wavelengths so long after impact, it is not surprising that only McGregor *et al.* (1996) reported the effect. The model does not perfectly fit McGregor's ring, producing radii 35% too large and offsets 50% too large, but this may be because it is an inviscid model. One of us (Deming) has calculated that molecular viscosity in the strong shear between the sliding plume and the stationary atmosphere (the 0.01–0.1 mbar level) can provide much of the friction required to slow the plume, depending on the details of the shock structure. Turbulent viscosity may also be important. If, as we expect, other parameters such as the total plume mass do not strongly affect the sliding distance, McGregor's

ring may place limits, or actual values, on upper atmospheric turbulence in a regime not easily probed by other methods.

8.3.5   Cooling and Dissipation

The dissipation phase begins when motions have generally returned to their pre-impact patterns. The impact sites cooled in a few days, quicker than expected for the unpolluted atmosphere (Bézard 1997, Fast *et al.* 2002). Fast *et al.* saw elevated temperatures at µbar levels a day after the G impact and over a distinctly deeper region (>200 µbar) 4 days after the impact. Bézard (1997) report excess heat over the smaller E site 2.6 days after impact. Temperature enhancements over the large and some of the medium impacts (G, K, L, W-Q1, R) were no longer clearly detectable in the thermal infrared a week after the impacts (Kostiuk *et al.* 1996, Bézard 1997). From time-dependent radiative modeling, Bézard (1997) proposed that sub-micron silicate particles were responsible for this enhanced cooling. Moreno *et al.* (2001) also point out that temperatures 10 K colder than pre-impact conditions were derived from observations made 2–3 weeks after impact. Overcooling may be due to exotic infrared radiators (e.g., H_2O).

The winds advected SL9 particulates, and those with sub-micron sizes remained in the stratosphere for years (Sanchez-Lavega *et al.* 1998). This longevity, and the particulates' injection by a series of discrete events at discrete times, made them ideal probes of stratospheric winds and eddy turbulence. At the impact latitude, tropospheric zonal wind speeds are typically $35 \, \mathrm{m \, s^{-1}}$ (Limaye 1986). A thermal-wind analysis of horizontal temperature variations measured by *Voyager* implies that Jupiter's winds decay with height above the cloudtops (Gierasch *et al.* 1986). Banfield *et al.* (1996) found that tracking SL9 dust gave zonal winds at the 10-mbar level that were reduced from the tropospheric values by factors of 2.5 to 6, roughly consistent with the vertical shear calculated by Gierasch *et al.*. In principle, vertical zonal wind shear could be measured directly from the SL9 impact patterns by tracking particles of different sizes that have reached different depths. In practice, Banfield *et al.* found that their retrievals of particle height profiles were not sufficiently unique to enable direct wind shear measurements. Simon and Beebe (1996) found that turbulent circulation within a specific storm system does not decay with altitude in the manner of the zonal winds.

Spreading of the SL9 dust in latitude reveals the atmospheric meridional transport, which is important to atmospheric dynamics and is virtually impossible to measure otherwise. Friedson *et al.* (1999) found that the SL9 dust moved equatorward by 25° in 3.2 years. Their model of advection by the residual circulation (the sum of eddy transport and a zonally-averaged Hadley cell) predicted a poleward motion that was many times slower. Friedson *et al.* were able to obtain agreement with the observed motion patterns only by including an eddy diffusivity that varied spatially between 3×10^9 and $3 \times 10^{10} \, \mathrm{cm^2 \, s^{-1}}$.

The SL9 events did not affect long-term tropospheric dynamical systems (e.g., vortices and zonal jets), nor were they expected to (Harrington *et al.* 1994). However, see Section 8.4.3 and Chapter 7 for the long-term picture in atmospheric chemistry.

8.3.6   The HST Rings

HST images of several impact sites show expanding, narrow rings that look like waves (Figure 8.6, HAM95). Waves are exciting because they reveal properties of the media in which they propagate: seismologists use them to map the interior of the Earth, for example, and atmospheric scientists use them to infer the vertical structure of an atmosphere. Dowling (1995) assumed a gravity-wave interpretation for the HST rings and then used Arnol'd's second stability criterion to predict the deep winds based on the rings' speed. Extrapolating Dowling's plot to the *Galileo* Probe entry latitude gives a speed very close to that later found by the Probe at depth. However, there are many models that fit the ring data, and there are additional tests that might distinguish among the models but that have not been carried out. In this section we summarize the observations, discuss what kinds of models could apply, review the models that have been published, and describe an approach to deciding this open question.

After impacts A, E, G, Q1, and R, an outer ring expanded at $454 \pm 20 \, \mathrm{m \, s^{-1}}$. The largest observed radius was 4649 km (still inside the crescent) at 2 hours, 22 minutes after impact. McGregor's ring was then $\sim 20\,000$ km in radius. The E and G events show a fainter second ring moving at 180–$350 \, \mathrm{m \, s^{-1}}$. Ring radii plotted *vs.* time show linear expansion, with little if any deviation for different events (HAM95). The outer ring's fit to combined data extrapolates to a radius of 586 ± 125 km at impact time. The disturbance thus either propagated faster in the 50 minutes before the first image or the rings originated from a circular disturbance over a relatively large region centered on the impact site, such as the reentering plume. The smaller ring's less-certain fit could have intercepted the origin, so a simple, constant-speed model is conceivable. The rings, crescent, and streak were all dark at continuum wavelengths against the sunlit clouds, but they were bright in CH_4 absorption bands, indicating that material was at least partly above the 380-mbar level (West *et al.* 1995). The rings always appeared inside the crescent, but they propagated past the stationary streak. Their narrow widths hid them from ground-based view.

There are three phenomena to explain: visiblity, propagation, and genesis (the coupling of impact energy to the propagation mechanism). Possible visibility mechanisms include convergence of particulates or condensates in the flow field of a wave peak, condensation in a wave peak or trough, a refraction effect, or horizontal transport (advection) of dark material. A refraction effect would need to diminish light from below and enhance light from above just as did streak and crescent material. We find this improbable at best, but there are arguments both for and against each of the other three options. Gravity (buoyancy) waves are a clear candidate for the propagation mechanism, since plausible speeds include the rings' speeds. Impact and plume splash models (Figures 8.1 and 8.11) generate shocks, but sound velocities are $\sim 1 \, \mathrm{km \, s^{-1}}$ at 200 K on Jupiter, rising to over $3 \, \mathrm{km \, s^{-1}}$ in air heated by plume reentry shocks. These waves are too fast. There are numerous potential genesis mechanisms, such as the passage of the bolide or the plume through the atmosphere and the reentry of the plume.

Prior to impact, Harrington *et al.* (1994) predicted 400

$\mathrm{m\,s}^{-1}$ gravity waves in the stratosphere as the main observable effect of an impact on the general circulation. The model sacrificed vertical resolution to achieve global coverage, but this caused its sponge layer to act like a rigid lid that slowed gravity waves in the stratosphere (Ingersoll and Kanamori 1995; sponge layers suppress unphysical wave reflections from a model's top surface). Subsequent work using the same numerical code but with more layers (Dowling 1995) showed stratospheric gravity wave speeds of about 900 $\mathrm{m\,s}^{-1}$, as did other gravity-wave models that were in development prior to the impacts. The 454 $\mathrm{m\,s}^{-1}$ observed speed thus required adjustments to the existing gravity-wave models.

Ingersoll *et al.* (1994) and Ingersoll and Kanamori (1995, 1996, collectively IK) adjusted their static stability (stratification) profile to emulate an enriched H_2O cloud (the profile is sensitive to deviations from an adiabatic thermal profile). They emphasize that Jupiter's atmosphere normally features two classes of gravity waves. In the stratosphere, they argue that the linear gravity wave speed is 930 $\mathrm{m\,s}^{-1}$, and that it is difficult to change this speed. However, high static stabilities that would produce a gravity waveguide have been widely expected in the putative tropospheric H_2O clouds (Allison 2000, IK). Ingersoll *et al.* (1994) predicted a wave velocity of 130 $\mathrm{m\,s}^{-1}$ in this waveguide for solar abundance of oxygen (and therefore H_2O). To raise the tropospheric wave velocity to 450 $\mathrm{m\,s}^{-1}$ requires raising the static stability by the same factor, which in turn requires raising the oxygen abundance by a factor of ~ 10.

IK's provocative conclusion fueled much of the interest in the HST rings. It pushes hard against upper limits for the mass of heavy elements in Jupiter (42 Earth masses, Chapter 2), and it exceeds the upper limit of 7.5× solar for the mass fraction outside the core (Guillot *et al.* 1997). Volatile abundances obtained by the *Galileo* Probe in a cloudless hot spot indicate that N, C, S, Ar, Kr, and Xe are all roughly three times solar (Mahaffy *et al.* 2000, Owen *et al.* 1999). The derived oxygen abundance may better represent the dry entry location than the planet as a whole, so one may suspect that H_2O is also three times solar. However, the uniform enrichment of most volatiles is not yet explained (Chapter 2), so greater enrichment of H_2O on Jupiter is not (yet) ruled out. The *Galileo* Probe also directly measured tropospheric static stabilities in a cloudless hot spot of $\sim 3 \times 10^{-3}\ \mathrm{s}^{-1}$ (Magalhães *et al.* 2002, but expressed as Brunt–Väisälä frequency, N). These are similar to what IK used for solar abundances of H_2O in the waveguide, but again that measurement may not represent the profile in wetter regions of Jupiter.

IK's tropospheric gravity wave produces a ~ 1 K temperature perturbation at 45 mbar, 1–2 orders of magnitude stronger than their stratospheric gravity wave. They argue that the wave is more likely made visible by condensation than advection, but do not consider convergence.

Zahnle (1996) suggested that the rings were nonlinear stratospheric gravity waves analogous to tidal bores. Such waves were produced by the rising, buoyant plume in the numerical models of Zahnle and Mac Low (1995), and had the right velocity to explain the observed rings. However the numerical rings failed to propagate far enough or for long enough times to explain the data. Efforts to coax the numerical model into generating longer-lasting rings were unsuccessful.

Walterscheid *et al.* (2000) developed a stratospheric gravity wave model that reproduced the observed ring velocity in a nominal atmosphere without a moisture-induced waveguide in the troposphere. They force waves by heating Gaussian footprints <1000 km in diameter, mostly above 1 bar, over 2.5–10 minutes. Their leading wave's speed is 802 $\mathrm{m\,s}^{-1}$, but it may be too weak to observe. Waves at 475 $\mathrm{m\,s}^{-1}$ and 356 $\mathrm{m\,s}^{-1}$ have speeds close to those observed and could be strong enough to see. Walterscheid *et al.* favor convergence to make the rings visible, and they are the only modelers who discuss optical visibility quantitatively. The nominal model produces about a 10% particulate number-density enhancement. They state that a tenfold enhancement would be possible, but they do not show that this would make the rings dark enough. Their 753 $\mathrm{m\,s}^{-1}$ divergent wave could be mapped onto the clear region preceding the outer ring. A test of their model would be to show that the clearing's outer edge grows at the speed they predict. Walterscheid *et al.* (2000) ran their model with the IK temperature profile and also found significant ducting, but only if they used a rigid lower boundary. With a deep adiabatic lower layer in the model, the waves sped up and the amplitudes decreased.

The Walterscheid *et al.* (2000) model is perhaps the most successful to date, but it still has several weaknesses. The wave speeds are sensitive to the size of the forcing region, a free parameter. Walterscheid *et al.* attribute the forcing to plume infall, but apply it at an unrealistically deep level. Deming and Harrington (2001) show that plume infall effects do not extend below 1 mbar (Figure 8.11), and they did not see the Walterscheid *et al.* wave in their model. Deming and Harrington point out that the primary effect of the splashback (apart from the shock heating) is to produce an external pressure on the atmosphere. Although this may induce a pressure-mode oscillation of the atmosphere (e.g., at the acoustic cut-off frequency), the splashback itself would be inefficient at exciting internal gravity waves. Also, the real atmosphere was significantly perturbed by the events, unlike the model atmosphere. Shock heating above 1 mbar produced transient but very high static stabilities and a very strong waveguide at the same altitudes where one expects to find the material that renders the disturbance visible.

There are numerous unmodeled possibilities and many open questions. Jupiter's condensates are usually bright, so why are the rings narrow and dark? Which impact phenomenon produced the rings? If they are waves, how much energy did they carry? Why did they cease to be visible? Why were McGregor's ring and the many modeled shocks not seen in the HST images? A believable model must combine genesis, propagation, and visibility mechanisms to produce synthetic images that quantitatively match the observations. It must also show why the other suggested propagation mechanisms either do not apply or do not produce visible rings.

8.4   ATMOSPHERIC CHEMISTRY

The SL9 events generated molecules (Table 8.2) and dust (Table 8.3) that were unusual for Jupiter. Some were observed at high temperature during the main event; most have also been observed post-impact, after cooling. In general,
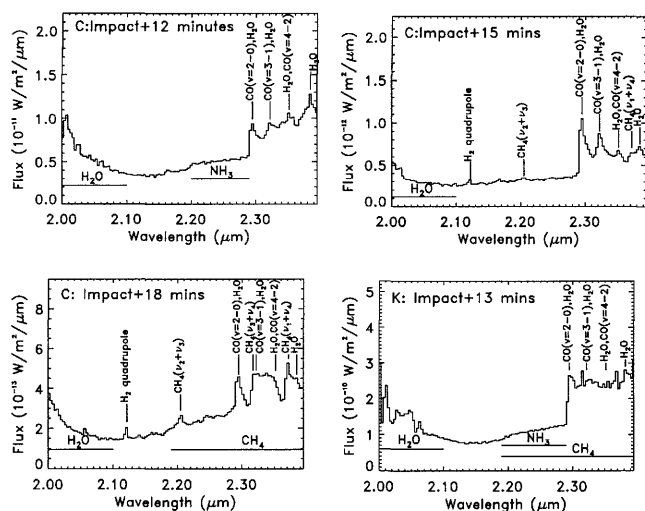
Figure 8.12. Identification of emitting species observed during the plume reentry phase for the C and K events. Time after impact is indicated on each of the panels. Wavelengths for water features identified are valid for H_2O at $T < 1000$ K. Reprinted from Meadows et al. (2004).

the products represented either the comet's composition or processes specific to the event phenomena. For Jupiter itself, the chief points of interest are what the impacts might have excavated from the troposphere and what role cometary impacts may play in governing stratospheric abundances of CO, CO_2, and H_2O (Bézard et al. 2002, Lellouch et al. 2002). The latter comes about because the stratospheric lifetimes of these molecules can be very long (Moses 1996), so that rare, large events can dominate the accounting. One should also not forget that impacts much larger than the SL9 events may have unexpected consequences.

8.4.1 Main-Event Observations

Several ground-based observers obtained near- and mid-infrared spectra of the main event (Bjoraker et al. 1996, Dinelli et al. 1997, Encrenaz et al. 1997, Fitzsimmons et al. 1996b, Herbst et al. 1995, Knacke et al. 1997, Meadows et al. 2001, 2004, Nicholson et al. 1995a, Roos-Serote et al. 1995, Sprague et al. 1996), as did the *Galileo* Near-Infrared Mapping Spectrometer (NIMS, Carlson et al. 1995). The same five molecular species, CH_4, H_2O, NH_3, CO, and H_2, appeared in both the C and K event 2.0–2.4 μm spectra (Figure 8.12). Although they account for most features in the C spectra, they do not account for all features in the K spectra. The unidentified features are either due to additional species or to the identified species at many different temperatures.

Main events typically started 6–7 minutes after impact. Dinelli et al. (1997) report 3.5-μm CH_4 emission at 1400 K for the C event, cooling to 1150 K at 8 minutes after impact. Meadows et al. (2004), agreeing, recorded 2.0–2.4 μm spectra dominated by line emission from H_2O, CH_4, and NH_3 at ~1000 K. CH_4 emission peaks 8–10 minutes after impact at 2.2 μm for the C event (Meadows et al. 2004), and 9 minutes after the R impact in KAO spectra taken between 6 and 9 μm (Sprague et al. 1996). In the C event

CH_4 cooled gradually from 1000 K to 660 K, 19 minutes after impact (Dinelli et al. 1997). H_2O emission peaked at 13 minutes for the mid-sized C, H, R, and W events and at 14 minutes for the larger G and K events (Bjoraker et al. 1996, Herbst et al. 1995, Meadows et al. 2004, Sprague et al. 1996). H_2O may have been cooler than CH_4; the highest reported temperature was 1200 K (Bjoraker et al. 1996), but H_2O temperatures generally were at or below 1000 K.

Strong, hot CO emission, on the other hand, appeared abruptly at 2.30 μm, 12–13 minutes after impact, reaching peak strength 1–2 minutes later (identified with the flare at the end of the main event), and faded away over the next 10 minutes. During this time CO dominated the 2.0–2.4 μm spectrum. Profiles and bandhead wavelengths of the CO 2–0, 3–1, and 4–2 bands indicate rotational temperatures of 1500–2500 K for six of the impacts (Meadows et al. 2004). However, Kim et al. (1999) reported CO temperatures as high as 5000 K, 873 after the R impact. Hot NH_3 produced an emission plateau between 2.2 and 2.3 μm in the minutes before the first appearance of CO, but it disappeared thereafter. Quadrupole emission from H_2 (2.122 μm) appeared approximately 18–19 minutes after impact in the C, D, G, H, and K events only, becoming successively more difficult to detect. The strong appearance of this feature only in the earlier events is consistent with the ejecta being concentrated closer to the planetary limb, providing a larger path length for H_2 emission. When H_2 was detected, CH_4 emission between 2.2 and 2.4 μm reappeared strongly in the spectrum. At 16–21 minutes after the L impact, Fitzsimmons et al. (1996b) saw strong optical atomic lines from NaI, FeI, CaI, MgI, MnI and CrI, which they interpreted as the meteoritic ablation of reentering grains. The relative strengths of the FeI multiplet 1 and 2 emission demonstrate a rapid rise in the excitation temperature from 1500 ± 100 K to 1800 ± 100 K and an increase in column densities by a factor of 10 over this period. Spatial variations in emitting species were also observed across the C impact site, with H_2 and CH_4 most prominent at the edges of the ejecta. Shock waves are likely the source of these distant emissions, consistent with the observations of McGregor et al. (1996) and the model of Deming and Harrington (2001).

Radiative transfer modeling of the observed spectra indicates that ejecta containing nominal CH_4 abundances would have produced far more emission than was observed. This would imply either strong CH_4 self-absorption or depleted CH_4 in the ejecta. CH_4 and H_2O emission lines in this spectral region also form a pseudo-continuum at the spectral resolution of the data, reducing (but not eliminating) the need for particulate emission to explain the observed continuum.

Significant events in the spectra correlate with those in the light curves. For example, 7–8 minutes after the C impact, the light curve, which had been rising rapidly, starts to flatten out and rise more gently. Simultaneously, the spectra, which were previously dominated by CH_4 absorption, now lose all signs of absorption. They instead show a pattern characteristic of emission from CH_4 at temperatures close to 1500 K (consistent with the Dinelli et al. 1997 estimate of 1400 K at this time). Ballistic calculations (Meadows et al. 2004, Nicholson 1996) imply that this was the time when ejecta from the C impact site first began to fall directly on the limb and visible hemisphere of Jupiter.

Table 8.2. Observed SL9 chemical products.

Species	Event	Mass (g)	Pressure (mbar)	Temperature (K)	R/O	Source(s)	Comments	Ref.
CO	K	1.5(14)	<0.1		all	comet	cools quickly	L97
	R			>2000				Kn97
	R			2000–5000			$8 < t < 14$ min	Ki99
	G	0.5–2(14)						M01
	C, K						$13 < t < 25$ min	AAT
	total	7.5(14)	<0.1				scaled from K	L97
H_2O	G	3–10(12)	<10	1000	O	comet	temp $t = 14$ min, mass $t = 40$ min	Bj96
	G	0.6–2.8(12)					lower limits	E97
	R	0.1–1.3(12)					lower limits	E97
	C, K			700			cools quickly	AAT
	total	5(13)	<1				$t > 3$ years	L02
CO_2	G, R	<5(11)			O	comet	$t = 9$ min, upper limit	E97
	total	⩽4(12)	<0.1				$t = 0$, inferred	L02
	total	1.4(13)	<1			$CO+H_2O+h\nu$	$t > 3$ years	L02
S_2	G	1(14)			N	comet?	superceded by Y96	N95
	G	4(10)	<0.1	1200			disappears in days	Y96
	total?	7(11)					review	L96
CS_2	G	3(10)			R	Jupiter?	UV bands, t>1 month	N95
	G	1.5(11)	1–10				review	L96
	G	1 (11)	<0.1					Y96
CS	G	3(9)			R	Jup., comet	UV	N95
	G, S	>9(9)					UV, $t = 45$ min, 3 days	L96
	K	5(11)	<1				mm wavelengths	L96
	K	0.4–1.7(12)	<1					M01
	Q, R, S	0.9–2.5(12)	<1					M01
COS	W, K	3(12)	<1		N	comet	one detection	L96
H_2S	G	<3(12)	5–100		R	air	detection disputed	L96
HCN	G	1(12)	<0.1		R	Jupiter, comet		L96
	K	7(11)						L96
	E	6(11)	<0.1					L96
	K, W	2(12)						Be97b
	L, G	5(12)						Be97b
	G, Q, R, S	4(12)						Be97b
	E	1(12)						Be97b
	H	4.5(11)						Be97b
	total	1.1(13)						Be97b
N_2		–			all		undetectable	
NH_3	C, K			<1500	R	air	$t < 13$ min	AAT
	K	2(13)	1–20				1–12 days, spreading	G97
	total	1.5(14)					$t = 8+$ days	Be97a
	total	<4(12)					$t = 9$ months	Be97a
	Q1	1(12)	<10				$t = 8+$ days	L96,K96
	G	1(11)					UV bands, $t >$ months	N95
	G	>2(13)	<0.003	283			$t = 1$ day	Fa02
	G	>1(13)	<0.2	204			$t = 4$ days	Fa02
CH_4	many	large	many	750–1500	R	air	hot CH_4 seen	L96,K96
	L		0.005	$\Delta T = 80$			$t = 11$ hours	Be97b
	L		1	$\Delta T = 20$			$t = 11$ hours	Be97b
	L		5	$\Delta T = 10$			$t = 11$ hours	Be97b
C_2H_2	E	≪3(13)	0.003	208, $\Delta T = 37$	R	Jupiter	excess emission detected	Be97b
	K, W, Q1		0.003	$\Delta T < 13$			attributed to heating	Be97b
C_2H_4	K	3(12)	<0.1		R	Jupiter	>1000× normal Jupiter	L96
	K	1(12)						G97
H_2	C, K		<1	>2000	R	air	$13 < t < 40$ min	AAT
PH_3		??	1		R	air	reported	L96
SO	G	<1 (11)			O		not detected	N95
SO_2	G	<3 (11)			O		not detected	N95

Mass: a(b) = a × 10[b], R/O: R = reducing, O = oxidizing, N = neutral, air = unprocessed, Jupiter = processed, ΔT = perturbation above normal for given pressure, t = time after impact, hν = photochemistry, AAT = Meadows *et al.* (2004), Be97a = Bézard *et al.* (1997a), Be97b = Bézard *et al.* (1997b), Bj96 = Bjoraker *et al.* (1996), E97 = Encrenaz *et al.* (1997), Fa02 = Fast *et al.* (2002), G97 = Griffith *et al.* (1997), K96 = Kostiuk *et al.* (1996), Ki99 = Kim *et al.* (1999), Kn97 = Knacke *et al.* (1997), L96 = Lellouch (1996), L97 = Lellouch *et al.* (1997), L02 = Lellouch *et al.* (2002), M01 = Moreno *et al.* (2001), N95 = Noll *et al.* (1995) Y96 = Yelle and McGrath (1996).

Table 8.3. Observed SL9 dust.

Event	Mass (g)	Pressure (mbar)	Temperature (K)	R/O	Source(s)	Comments	Ref.
total	7(14)	1–200				$r = 0.1$–0.3 μm	W96
silicate	3(14)	1–200		all	comet		W96
K, silicate	8(12)	<0.1		all	comet		G97
organic	4(14)	1–200		R	comet, Jupiter	= total − silicate	
R, silicate	6(12)	<20	400	all	comet		Ni95
E, H, L, R			600			color temperature	Ni96
total	1(15)	<20				$r = 0.25$ μm	Ba96
R	1–5(12)					silicates, $r = 0.1$ μm	WS97
generic	0.8–8(13)					organics,	WS97
big rings	1(10)						WS97
H						$t = 2$ hr, $r = 0.15$ μm	M97
core		300–450					M97
crescent		1–450					M97
G						$t = 13$ hr, $r = 0.2$ μm	M97
E, H					comet	$r = 0.05$ μm	Be97
E, H						H 4× dustier than E	Be97
total	1(15)					scaled from E & H	

Mass: $a(b) = a \times 10^b$, R/O: R = reducing, O = oxidizing, N = neutral, r = dust particle radii, t = time after impact, Ba96 = Banfield *et al.* (1996), Be97 = Bézard (1997), G97 = Griffith *et al.* (1997), M97 = Molina *et al.* (1997), Ni95 = Nicholson *et al.* (1995a), Ni96 = Nicholson (1996), W96 = West (1996), WS97 = Wilson and Sagan (1997).

8.4.2 Cooling Impact Sites and Modeling

Impact-driven chemistry can be divided into two regimes, an initial fireball phase with strong shock heating at high pressures and a later phase of high temperatures at low pressures when the plume reenters the atmosphere. Peak shock temperatures decrease as the shock wave advances, so that the fireball can be pictured as nested shells of shocked air. Using the energy- and momentum-distribution arguments of blast wave theory (Zel'dovich and Raizer 1967), Zahnle and Mac Low (1994) estimate that $(55\,000 \text{ K}/T') \times (\mu/2.5 \text{ g mol}^{-1})$ impactor masses are shock-heated heated above T', where μ is the molecular mass of the gas. Depending on the molecules present, some 30–50 impactor masses of air are heated strongly enough to drive thermal chemistry. This estimate applies to a massless explosion in spherical symmetry in a gas of constant density, and it neglects mixing. Mixing increases the amount of heated material, while the expanding plume takes energy away. The degree of mixing between comet material and air is unclear.

Much of the strongly shocked and some of the weakly shocked material goes into the plume. Adiabatic cooling as the plume expands reduces temperatures to tens of K; possibly even CH_4 and CO condense before reentry. When the plume reenters the atmosphere (the main event), it contains cometary material and about 10–30 comet masses of shocked air. By this point the plume is enormous and its density is correspondingly low ($<10^{-9}$ g cm^{-3} 5 minutes after impact) so that shock pressures are also low ($\ll 1$ mbar). As the main event unfolds, shock pressures generally decrease while the increasing reentry velocity makes temperatures increase. Ambient air is also shock-heated by the falling plume (Figure 8.11).

Silicate, Al_2O_3, and other grains form in the plume, providing the material observed in the visible images (Friedson 1998). They partially ablate in the ejection and reentry shocks, explaining observed emission by Mg and Na starting several minutes after impact (Moses 1997). Sub-micron particles tend to remain in the plume, but much larger condensates would penetrate the reentry shock and behave as meteors in the otherwise-undisturbed stratosphere. Loosely put, this means rocky particles >10 μm and icy or carbonaceous particles >100 μm in diameter, although details depend on the distance from the impact site. Most of the observed particles were sub-micron-sized (Table 8.3).

A third phase of plume evolution begins once the gas cools enough to become hydrodynamically unstable. This appears to have happened within hours. The dusty, CO-rich plume is naturally denser than Jupiter's air, and it also contains better radiative coolants. Hence, the plume materials will over time sink and mix with ambient air until they are sufficiently diluted that they no longer play a dynamical role.

The last of the important effects to consider is upwelling into the cavity left by the exiting plume. This appears to have happened with NH_3 in the G and K events. The quantity reported (2×10^{13} g, Griffith *et al.* 1997, Fast *et al.* 2002) is modest, and could be accounted for by just 20 impactor masses of air lifted from below 2 bar. If the source were instead the upper troposphere (0.6–2 bar), it would require 200 impactor masses, corresponding to $T' \approx 270$ K of shock heating. NH_3 abundances fall off rapidly at lower pressures. It therefore appears that the large G and K impacts excavated air from below the ∼1-bar level.

The chief source of most species in Table 8.2 is ambiguous, since most can be synthesized as easily from atmospheric constituents as from the comet. In particular, it is difficult to tell whether the impacts penetrated deeply enough to excavate sulfur. It does not appear that any of the impacts reached the water clouds at 5–8 bar (Bjoraker *et al.* 1996).

Sub-micron dust was one of the chief products, by mass, of the SL9 events. It is generally agreed (Table 8.3) that the particles were small (<0.3 μm diameter) and the total volume of dust was 0.5–1×10^{15} cm^3. The dust was optically

Table 8.4. SL9 chemical model results.

Species	Observed Amount (g)	Comet Fraction[a] 3% (g)	Comet Fraction[a] 20% (g)	Best Guess[b] Mixed Plume (g)	Air[c] Wet (g)	Air[c] Dry (g)	Comments
CO	7.5(14)	1(15)	7(14)	9(14)	2(14)	6(10)	
H_2O	5(13)	-	2(14)	1(14)	4(14)	2(10)	
CO_2	<4(12)	-	3(11)	2(11)	4(12)	-	
S, S_2, S_8	4(12)	1(11)	3(13)	2(13)	9(12)	1.4(12)	elemental sulfur
CS_2	1(12)	2(10)	-	1.4(11)	2(10)	2(13)	under-predicted?
CS	2.5(12)	1(14)	-	4(13)	-	2(13)	over-predicted
COS	1.5(13)	2(9)	4(10)	9(10)	3(9)	-	under-predicted
H_2S	<3(13)	-	-	-	5(13)	4(13)	survives upwelling but does not survive in plume
HCN	1(13)	1(14)	-	3(13)	7(9)	4(13)	does not seem to be a product of the comet
N_2	-	1(14)	9(13)	1(14)	2(13)	5(12)	
NH_3	1(14)	1(9)	4(9)	>2(9)	3(13)	2(13)	survives upwelling but does not survive in plume
CH_4	?	4(13)	-	>6(12)	8(13)	1.6(14)	amounts of hot CH_4 not reported
C_2H_4	5(12)	3(13)	-	5(12)	1(12)	1(12)	made in weakly shocked parts of fireball
SO	-	-	2(12)	6(11)	3(8)	-	
SO_2	-	-	2(13)	1(13)	2(13)	-	does not match data

[a] Products from fireball models with given mass fraction of comet *vs.* entrained air

[b] Average of fireball models with comet fractions from 3-50%

[c] Atmospheric reentry models with 0% comet

similar to other carbonaceous, high-altitude dusts on Jupiter (West 1996). Based on spectral features, Nicholson *et al.* (1995a) estimated that the R event generated 6×10^{12} g of silicate dust, from which West (1996) estimates that the dust was ~10–20% silicate by volume. This implies it was ~25–40% silicate by mass. The dust could be cometary, either synthetic or surviving, or generated by shock-heating of atmospheric CH_4. The silicates clearly came from the impactors.

The other major product was CO (Lellouch *et al.* 1997), about $5-8 \times 10^{14}$ g of which were injected into the stratosphere, a quantity sufficient to have long-term implications for Jupiter (Section 8.4.3). In the days and weeks after the impacts, CO remained above 100 μbar, which implies that the plumes distributed CO, either as a gas or in small grains. The theory is simple: CO is a major product of high temperature shock chemistry in any gas with C and O in it, tending to form until one of these is exhausted. CO could come from cometary materials by reacting H_2O with organics. Both excess H_2O and excess carbonaceous material (presuming some of the dust to be cometary) were left over. CO could also have been generated efficiently from wet air, or from atmospheric CH_4 using any remaining cometary H_2O.

It is impressive that a parent comet with a mass of ~1×10^{15} g should generate ~1×10^{15} g of sub-micron dust and another ~7×10^{14} g of CO. A nominal comet may be 30% silicate by mass. There is enough CO to accommodate ~4×10^{14} g of H_2O ice and ~3×10^{14} g of carbonaceous matter, thus to first approximation reconstituting an unsurprising comet, although leaving no C for dust. Using nominal solar abundances (C/O = 0.5), a superheated comet reduces to 50% CO, 28% silicates, 7.5% N_2, 6.5% H_2O, and 2.6% sulfur. The amount of H_2O is sensitive to the assumed C/O ratio, which can be influenced by the comet's degassing history. Also, any carbon that partitions into carbonaceous dust is balanced by producing more water. Borunov *et al.* (1997) point out that H_2O is also sensitive to the fireball's temper-

ature; a hot fireball produces less water than a merely warm one. Given these uncertainties, the observed H_2O/CO ratio of 0.07 is quite reasonable for a combusted comet.

Carbonaceous dust could also have an atmospheric origin. If mixing is efficient, there is enough entrained CH_4 in the plume to reduce an originally oxidized comet completely. An impact in dry air could process up to 0.6 impactor masses of CH_4 (assuming $T' > 1200$ K and C 3× solar), much of which would likely become soot. On the other hand, different dust/gas ratios in the E and H events imply that much of the dust was cometary (Bézard 1997). Zahnle (1996) suggested that the onset of shock synthesis of soot at temperatures above 1200 K might simultaneously account for the sudden onset of the main event and the sharp inner boundary of the ejecta crescent (Figure 8.8, Harrington and Deming 2001).

Other reported chemical products of the SL9 events include HCN, CS, CS_2, S_2, and C_2H_4. Apart from H_2O and CO_2 (if any, Lellouch *et al.* 2002), all SL9 chemical products were reduced or redox neutral. C_2H_4 is readily ascribed to shocked air. HCN can be attributed either to reduced enclaves in the comet or to atmospheric constituents. Either source can be quantitatively sufficient, given the modest amounts reported, but shocked, dry air is more productive. The excavation of NH_3 in the larger impacts suggests a largely atmospheric source for HCN. The first HST UV spectra showed spectacular, unanticipated bands of S_2 (Noll *et al.* 1995). Early reports assumed that the gas was at 300 K and thus overestimated the amount. Much less S_2 can generate the observed spectrum at more realistic temperatures of 1200 K (Yelle and McGrath 1996). The very low pressures and high temperatures of the reentering plume favor formation and survival of S_2 (Zahnle *et al.* 1995). All Noll *et al.* (1995) estimates for site G are tripled in Table 8.2 to account for material outside their aperture.

Sulfur chemistry presents problems. The observed sulfur species are reduced or neutral. They could be atmospheric or cometary. A 10^{15} g comet is ~3% sulfur by mass, more

than enough to account for the $<10^{13}$ g of sulfur actually reported. However, the absence of oxidized cometary sulfur remains puzzling given the survival of H_2O. Zahnle (1996) and Mac Low (1996) suggested on dynamical grounds that the large SL9 impacts reached the putative NH_4SH clouds. Most other modelers suggested that, if anything, the impacts went deeper (Section 8.3.1). Below the putative NH_4SH clouds, the atmosphere is $\sim 0.1\%$ S by mass (Niemann *et al.* 1998, based on H_2S abundance). Roughly 45 impactor masses of air are heated sufficiently $(T' > 1200\ \mathrm{K})$ to break down H_2S. Therefore we expect that the K event alone processed some 10^{13} g of atmospheric sulfur. This sulfur would be strongly reduced, which could supply CS and CS_2 but probably not S_2 or COS (Table 8.4). Like other condensibles, NH_4SH should have a very small scale height in its clouds, making sulfur yields sensitive to the depth of the impacts. CS and CS_2 especially should have varied greatly from big to small events. To our knowledge, no evidence of this sort has been reported, though analysis is complicated by the overlapping of impact sites. In all, not enough sulfur was observed to require a planetary source, but there is nothing to preclude one, either.

Lellouch *et al.* (2002) use post-SL9 observations to show that Jupiter's upper stratosphere currently contains about 4×10^{13} g of H_2O and about 1.4×10^{13} g of CO_2. The CO_2 is a photochemical product of CO and H_2O (Moses 1996), and so the original amount of H_2O injected into the stratosphere by the SL9 impacts was 5×10^{13} g. This is about 7% (by mass) of the CO. It is tempting to conclude that the survival of H_2O indicates that the comet had a slight global excess of O over C. But this would conflict with the rest of the chemistry, in particular the sulfur, and also with the different temperatures of CO and H_2O in the main event: if the CO and H_2O were well mixed, they should be at the same temperature. What is more likely is that the comet and its fragments were O-rich in some places and C-rich in other places. Large-scale inhomogeneity is emphasized by Bézard (1997), who notes that the dust/gas ratio in the H events was four times higher than the dust/gas ratio in the E event. The distribution of observed temperatures may also reflect the quality of the embedded radiative coolant. For example, a water-rich parcel may get no hotter than ~ 700 K, while a dry parcel might be cooled by CO radiating at 2000 K.

Hot CH_4, H_2, and NH_3 provide undoubted examples of shock-heated air. NH_3 is especially interesting because it is the one clear example of a planetary species being excavated from the troposphere and injected into the stratosphere. Observations indicate that hot CH_4 was seen before hot NH_3. Temperatures of 700–1500 K are reasonable. Hot CH_4 was seen throughout an event, but hot NH_3 was seen only during the first half of the main event. This could mean that NH_3 was ejected only at lower velocities, as befits its deeper source in Jupiter. But we also note that NH_3 is more fragile than CH_4 in shocked, dry air (Zahnle 1996). At higher temperatures N_2 and HCN form.

Table 8.4 compares predicted chemical products to observed totals. The model predictions are from Zahnle (1996). The observations are from Table 8.2 assuming that fragment K was 20% of the total impacting mass, G about 10%, and E about 5%. The model predictions are of two basic types. Columns 3–5 describe materials in well-mixed plumes generated out of the fireball itself. For example, column 3 describes the products of chemistry in a uniformly
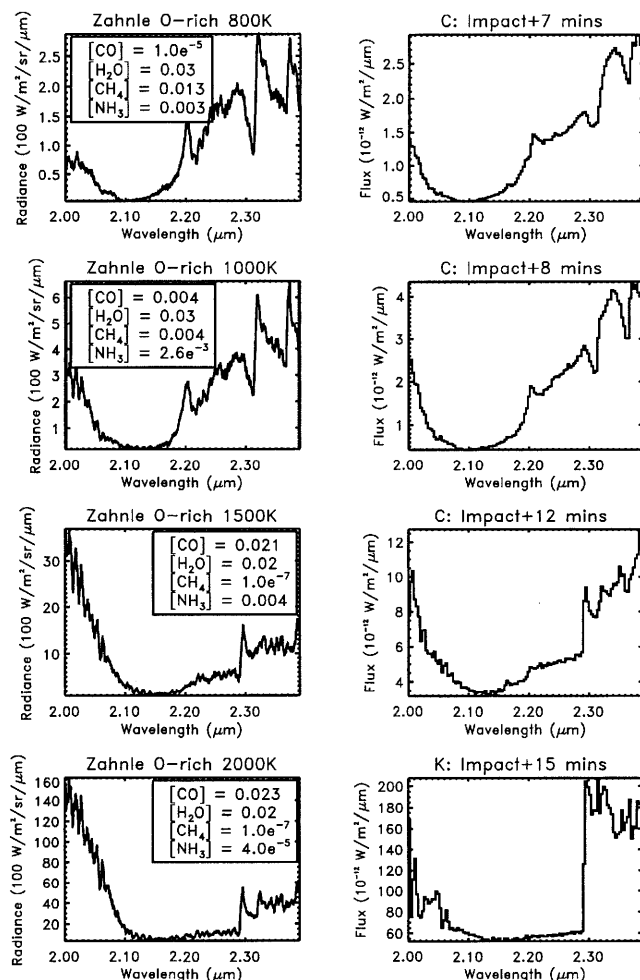
Figure 8.13. Comparison of observed spectra (right) with synthetic spectra (left). The synthetic spectra derive (Meadows *et al.* 2004) from O-rich splash model compositions as a function of peak shock temperature (Zahnle 1996, Figure 15). The early stages of the ejecta reentry are modeled with emission from CO, CH_4, H_2O and NH_3 at 800–1000 K (first two sets of panels). Although there is a good morphological match overall, in the range 2.32–2.36 μm there is an unexplained discrepancy. In the third set of panels (1500 K shock), the data and model both show the NH_3 plateau between 2.2 and 2.29 μm, and the sharp rise at 2.29 μm due primarily to hot CO emission. Water emission can also be seen at 2.29–2.40 μm, with a distinct feature at 2.385 μm, and at 2.0–2.09 μm. However, at the higher temperatures (1500–2000 K), the relative intensities of the two modeled H_2O emission regions do not match those observed. Decreasing the relative abundance of H_2O from the model values does not resolve this discrepancy. In the final set of panels (2000 K), note the sharp rise of the CO (2.295 μm) compared to the NH_3 plateau. The match of gross features and the evolution of features with time/temperature indicate that much of the variability observed is driven by chemical changes in the reentering ejecta as a function of increasing temperature. Reprinted from Meadows *et al.* (2004).

mixed plume that is 3% comet and 97% dry air by mass. Totals are normalized to the assumed mass of the comet (10^{15} g). The column labeled "Mixed Plume" averages together seven mixed plumes, of 3%, 5%, 6%, 7%, 10%, 20%, and 50% comet, with the total normalized to the mass of the comet. This mimics the shelled (onion-like) structure

produced around the terminal explosion by the decaying shock wave. The final two columns are different. These describe wet and dry air processed in the reentry shock, and are also averaged over the plausible range of shock temperatures and pressures. The models assume fully mixed materials at the level of free elements, with the silicates presumed condensed and not taking part in the chemistry. Additional model descriptions are given by Zahnle (1996) and Zahnle *et al.* (1995).

The models produce HCN and C_2H_4 from the atmosphere, not from the comet. The agreement between the predicted and observed quantities is quite good, which offers additional support for the estimated 10^{15} g mass of SL9. On the other hand, sulfur species are puzzling. The relative stability of S and S_2 radicals in the plume may be a model artifact – it is interesting that the model also under-predicts COS and CS_2, two species in which free sulfur is reasonably likely to accumulate. The oxidized sulfur species remain an embarrassment. The model predicts that SO_2 and H_2O should be tightly correlated. Only an inhomogenous comet (in which ices are stored separately from sulfur) and an ill-mixed plume (that keeps the sulfur and the water apart) can provide a resolution consistent with the model.

Spatially-resolved modeling with realistic air-parcel temperature/pressure histories from physical models may dramatically improve these results. Such physically-driven chemical models are also needed to interpret the time-varying spectra from the events themselves. Initial attempts to model the observed spectra by exploring the parameter space of temperature, shock altitude, and chemical abundances met with very limited success. However, the combination of these radiative transfer models with chemical models that predicted the mixing ratio of constituent species as a function of shock temperature produced spectra that were similar to observations (Figure 8.13). The most successful combination had an isothermal shock extending from 10 to 100 µbar. The prevalence of H_2O in the spectra of Meadows *et al.* (2004) provided strong evidence for an O-rich plume, so the mixing ratios came from the O-rich models by Zahnle (1996). While none of the synthetic spectra is an exact fit to the observations, the match of gross features and the evolution of these features with temperature/time is remarkable. Work is currently underway to tune these first-order models to determine the correct abundances of the constituents in the plume reentry.

8.4.3   Long-Term Implications

By 1997, impact-generated species had reached the equator (Lellouch *et al.* 2002), and during the *Cassini* flyby in 2000/2001, its Composite Infrared Spectrometer observed CO_2 in the southern mid-latitudes and in the south polar vortex (Kunde *et al.* 2004). Lellouch *et al.* (2002) present observations and a detailed model for the coupled photochemistries and transport dynamics of SL9-generated CO, H_2O, and CO_2. H_2O is lost on decadal timescales. CO is nearly immortal, removed by the putative eddy mixing and by limited photochemistry with H_2O (while there is a supply of H_2O) to form additional CO_2 (Table 8.2). Bézard *et al.* (2002) estimate that the e-folding time for removing CO from the stratosphere by eddy mixing is ∼300 years. They also suggest that comet impacts maintain a background level

of CO in Jupiter's stratosphere (Chapter 7, which also discusses long-term photochemistry). Chapter 18 notes that impacts and near impacts of comets have occurred fairly often in the historical record. A fair assessment of the data implies that km-size comets strike Jupiter about once a century. An event somewhat larger than SL9 is expected on the 300-year timescale of CO loss. Hence, large impacts should sustain a background level in excess of 10^{15} g of CO in the stratosphere. This is in good agreement with the background CO level inferred by Bézard *et al.* (2002) and is one of the major results of the SL9 analyses.

8.5   MAGNETOSPHERE

Predictions of magnetospheric effects from SL9 varied widely (see first *Geophys. Res. Lett.* special issue) because the perturbation was unlike anything previously observed, the energies were orders of magnitude beyond the range of human experience, and the events repeated about every 10 hours for a week. Cometary comae within a magnetosphere had not been observed, nor had surface explosions that blow through an ionosphere. The 10^{26}–10^{28} erg fragment kinetic energies dwarfed large volcanic eruptions (10^{23}–10^{25} erg) and nuclear explosions (10^{20}–10^{23} erg), and it was not even clear how our knowledge of such terrestrial perturbations would scale to Jupiter's vastly larger magnetosphere. The SL9 impacts thus offered a chance to observe a magnetospheric response to a high level of perturbation.

Atmosphere–Ionosphere–Magnetosphere Coupling

The coupling between the atmosphere, ionosphere, and magnetosphere took place via shocks, plumes, and precipitation of particles trapped in Jupiter's radiation belts. This coupling led to modification of the trapped radiation belts, placement of ionized material on to magnetic field lines, and a variety of emissions from the atmosphere in energy bands ranging from IR to UV to X-ray wavelengths.

The blowout produces a shock that precedes the plume into space. Ion–neutral collisions couple the shock to the ionospheric plasma. As the mean free path becomes long, the plasma supports the shock and the characteristic speed changes from the sound speed to the Alfvén speed. The planetary magnetic field provides the coupling mechanism necessary to maintain the shock. Such collisionless shocks also appear at the bow shocks of most planets and in interplanetary space. They interact with relativistic electrons, accelerating those that meet the energy threshold established by the shock. To form a collisionless shock, the ionospheric perturbation from the neutral shock must move faster than the local Alfvén speed. In Jupiter's quiescent ionosphere, the Alfvén speed is very high, ranging from a few × 1000 $km\,s^{-1}$ up to nearly the speed of light at altitudes of 6000 km, due to a combination of the high magnetic field strength and the low ionospheric density. This leads to one of two situations: if the perturbation is slower than the local Alfvén speed, large amplitude, nonlinear electromagnetic waves radiate the neutral shock energy into the ionosphere and magnetosphere. If it is faster, a collisionless shock forms.

During impact week the behavior gradually changed from the first case to the second. The Alfvén speed is a function of the mass of ions on the magnetic field lines. Ions and

charged dust carried up by plumes landed on field lines and decreased the Alfvén speed. Charged infalling coma dust is a major contributor to the field-line mass loading. This effect is cumulative, so the Alfvén speed decreased throughout impact week. The observed plumes (Figure 8.5) rose ∼3000 km above the limb (Jessup *et al.* 2000, HAM95), well above Jupiter's ionosphere, and optically thin material probably rose much higher.

Both collisionless shocks and electromagnetic waves created in the ionosphere significantly modified the magnetosphere. The plume itself also influenced the ionosphere and magnetosphere. The perturbed magnetosphere and ionosphere in turn lead to atmospheric effects through energetic ion and electron deposition. These depositions heated the atmosphere, emitted electromagnetic waves, and changed the chemistry of the upper atmosphere.

8.5.1   Observations

In this section we discuss observations made during and following the impact week. Following the impacts, changes observed in the atmosphere, ionosphere, and magnetosphere illustrated the interaction between these three regions. The data collectively form an extensive database for future research into radiation belt behavior and the effects of the ionosphere upon it. These data have already been used to propose and evaluate a variety of mechanisms that could explain the observed modifications, such as ionospheric current systems, collisionless shocks, and large-amplitude wave-plasma interactions (see, for example, reviews by Hill 1996 and Bolton 1997).

Ionosphere: IR, UV, and X-ray Wavelengths

HST, *Galileo*, and *Voyager* have imaged Jupiter's UV aurora in detail, and the IRTF has mapped H_3^+ line emissions (Chapter 26). These emissions are caused by molecular/atomic de-excitations, following excitation by auroral particle precipitation. Herbert (1994) predicted an intensification of the aurora and Io plasma torus, because the fresh surfaces of the comet fragments had been outgassing for ∼2 years before impact. Photo-ionization of this gas would create high-energy ions, which would intensify magnetospheric processes such as the Io plasma torus and aurora.

HST detected a brightening of Jupiter's ionosphere in UV images taken 47 and 57 minutes after the K impact. Bright emissions appeared near the conjugate footpoint of the field line that threads the impact location in unperturbed conditions. Fainter emissions appeared just south of the impact site (Clarke *et al.* 1995). Hill and Dessler (1995) suggest that these aurorae are driven by plume reentry. The infalling material (Section 8.3.4) drove diverging jets while plowing through the upper atmosphere. These jets generated current systems in the upper atmosphere, including magnetic-field-aligned Birkeland currents. The authors suggest that the field-aligned electrostatic potential drop associated with these Birkeland currents will accelerate the primary electrons that are responsible for auroral excitation. The Deming and Harrington (2001) plume reentry model supports Hill and Dessler's suggestion: their lateral shock (Figure 8.11) is quite similar to the snowplow shock required by Hill and Dessler.

Just before the P2 impact, HST detected two spots with significant UV emission inside the southern auroral oval. These spots were detected twice at 20 minutes intervals, and cannot be attributed to the P2 impact. Prangé *et al.* (1995) showed that these spots could be magnetically connected to the Q1 and Q2 fragments, which were about 7 R_J from Jupiter at the time. They suggest that enhanced particle precipitation was triggered via a current system generated by the relative motion between charged dust grains in the cometary coma and the local plasma (Ip and Prangé 1994).

Waite *et al.* (1995) reported ROSAT observations of enhanced X-ray emissions from the northern auroral region that occurred twice: once just prior to the K impact and again between the P_2 and Q_1/Q_2 impacts. Although the timing suggests a connection to the SL9 impacts, the brightenings were not at the longitude of the impacts, but appear at $\lambda_{III} \approx 170°–180°$, the region where X-ray brightenings usually occur in unperturbed conditions.

Between 22 and 31 July, infrared observations revealed intense H_3^+ emissions over the impact sites and anomalous H_3^+ emissions near the conjugate points of the impact sites (Schulz *et al.* 1995, McGregor *et al.* 1996, Miller *et al.* 1995). The latter emissions were particularly strong near the end of the impact week, while the H_3^+ emissions over the impact sites faded away over time. Miller *et al.* (1995) attributed the north/south asymmetry in the H_3^+ emission to a reduction of the conductivity in the southern auroral zone. This in turn was attributed to high altitude particulates or gas drifting southward from the impact sites at speeds between 50 and 100 m s^{-1} (Clarke *et al.* 1995). A decrease in the conductivity changes the ionospheric currents driven by plasma corotation, leading to an increase in the northern conjugate currents and a subsequent enhanced Joule heating of the northern auroral ionosphere, and thereby to enhanced H_3^+ emission there.

Auroral Regions: Decametric Observations

Decametric radio emissions originate near the auroral region in sequences of short (10^{-3}–1 s) bursts. This is coherent electron cyclotron radiation, emitted by electrons in the tens of keV range at their frequency of gyration around magnetic field lines. The radiation peaks near 8 MHz, and does not exceed 40 MHz, the gyrofrequency corresponding to the maximum magnetic field strength at Jupiter's cloudtops. Carr *et al.* (1983), Zarka (1992), Chapter 27, and others provide more specifics on this radiation.

Predictions for impact-induced changes in radio emissions focused on a possible increase in the frequency of radio bursts triggered via an electrical current system that would be generated through interactions between charged comet dust and the local plasma (Ip and Prangé 1994, Kellogg 1994, Farrell *et al.* 1994). No change in the frequency of burst occurrence was detected from the ground at 16.7–32 MHz (Carr *et al.* 1995), nor were changes in the radio emission at frequencies <1 MHz detected by *Ulysses* (Desch *et al.* 1995). A worldwide network of amateur radio astronomers, organized by Paul Harden at the National Radio Astronomy Observatory, listened carefully to Jupiter's emissions during impact week. They heard a noticeable decrease in intensity at frequencies above ∼18 MHz for ∼10 minutes at the time of the G impact (most observers used systems sensitive in
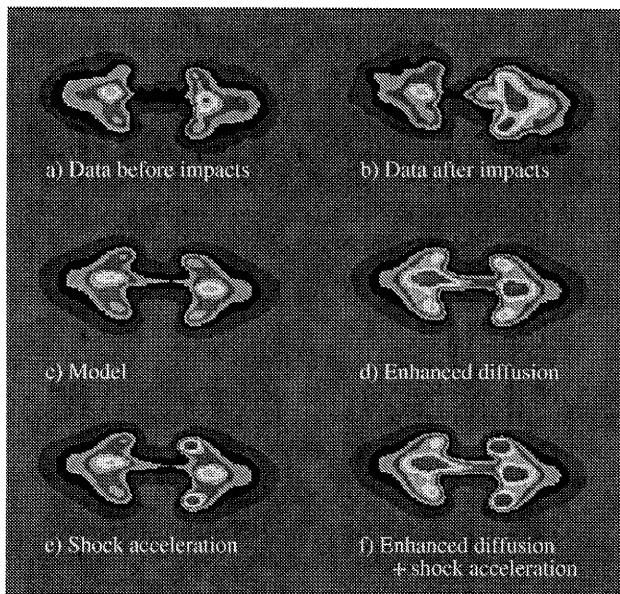
Figure 8.14. Real and model synchrotron emission images of Jupiter. (a) 20-cm pre-impact VLA data. (b) 20-cm VLA data taken after impact L. (c) Synthetic 20-cm image from the Brecht *et al.* (2001) model using the ambient relativistic electron distribution. (d) Synthetic 20-cm image with the diffusion coefficient enhanced by 3×10^6 compared to panel (c). (e) Synthetic image after the interaction of a shock with the particle distribution in panel (c). (f) Synthetic image using both the shock model and enhanced diffusion. Reprinted from Brecht *et al.* (2001), copyright © 2001, with permission from Elsevier.

the 18–30 MHz range). They also recorded 2–3 dropouts in the ambient radiation for the V and W events. Such a decrease in the continuum emission may arise from a general uplifting/rising of the ionosphere, effectively increasing the atmospheric loss cone of precipitating electrons. It could also be explained by a field-aligned current system, triggered by friction between the neutral wind in the atmosphere and the ionized gas near the impact site (Ip 1996, Hill and Dessler 1995). This would enhance particle precipitation, and hence would decrease the auroral radio emissions while increasing the ionospheric IR, UV, and possibly X-ray emissions.

Radiation Belts: Decimetric Observations

Jupiter's decimetric radiation was observed at wavelengths ranging from 3.5 to 90 cm, with a large fraction of the data taken at 20 cm. There were three rings of strong emission. Figure 8.14, panel a, shows a radio image of Jupiter's integrated synchrotron radiation from these rings at 20 cm under quiescent circumstances (Chapter 27, de Pater *et al.* 1997a, and others review the steady state of Jupiter's synchrotron radiation). This integration results in the rings manifesting themselves as peak regions to the left and right of the planet. The equatorial ring shows two intense regions, later referred to as the main peaks. The high-latitude regions are produced by electrons at their mirror points, bouncing up and down field lines at $L \sim 2$ (for a centered dipole, McIlwain's parameter, L, is the distance in planetary radii

from the planet's center to where a given field line crosses the equatorial plane).

Predictions of changes in synchrotron radiation ranged from complete disappearance to increased output. Dessler and Hill (1994) concluded that adding cometary dust would lead to no effect, while de Pater (1994) called for a significant decrease, depending on the dust column density. Brecht *et al.* (1995) argued that shocks might increase the emissions. Observations showed a small localized decrease in synchrotron emission followed by a substantial increase ($\sim$20% in the total intensity at $\sim$20 cm), and a hardening of the radio spectrum. The spatial distribution also changed drastically, as manifested both in images and in a flattening of the beaming curve (the variation in Jupiter's total intensity during a full rotation) (see, for example, the review by Leblanc *et al.* 1997). Changes in the spatial distribution are most clearly seen after application of the 3D tomographic reconstruction technique of Sault *et al.* (1997b, Figure 8.15). This technique has not yet been applied to all of the available data. The simpler back-projection technique (de Pater *et al.* 1997b) has been applied to much of the data.

Some impacts led to substantial changes in the synchrotron emission, while others did not. Observers generally saw the main radiation peaks brighten substantially more than the high-latitude regions during the first few days of impacts. This trend reversed mid-week, when the high-latitude regions intensified much more than the main radiation peaks. All emission regions moved closer to Jupiter during the events, while the high-latitude regions also moved to lower magnetic latitudes. The enhancements were never centered at the longitude of impact (de Pater *et al.* 1997b), but always trailed behind (Figure 8.16). The observed enhancements suggest the electrons drifted at a very slow rate in the direction of the usual ion drift rather than that of the electron drift. This observation appears consistent with the suggestion of Sault *et al.* (1997a) and Dulk *et al.* (1997) that the enhancements in the radiation regions stay coherent for much longer than normal drift theory would predict.

The displacement of the synchrotron radiation peak shown in Figure 8.16 is in the super-corotational direction relative to System III. This shift is therefore not an effect of mass loading, which would lead to sub-corotation and thus an opposite shift.

The papers by Leblanc *et al.* (1997) and de Pater and Brecht (2001b) present the evolution of all observed changes in the synchrotron radiation. Section 8.5.2 discusses highlights of explanations by various researchers.

Io Plasma Torus: Visible and UV Wavelengths

Io's plasma torus has been monitored for many years from the ground in the SII emission line and from space in the UV (Chapter 23). Predictions of what might happen to the Io plasma torus during the events varied from no effect (Dessler and Hill 1994), to a considerable brightening of the torus due to pickup heating of cometary materials in the outer magnetosphere (Herbert 1994), to a decrease in torus rotation due to a decrease in Jupiter's ionospheric conductivity (Cravens 1994). There were no changes in plasma torus density, ion temperature, or rotation velocity larger than the normal day-to-day variations (Brown *et al.* 1995). Observations in the UV are generally consistent with these conclusions
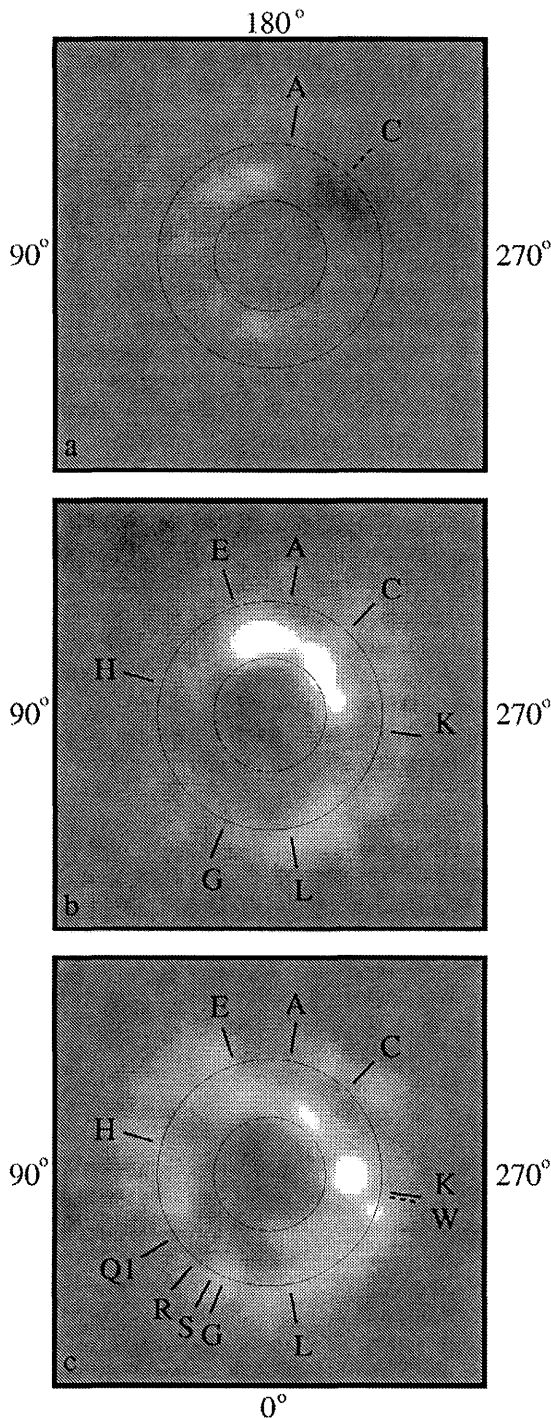
Figure 8.15. A 3D tomographic reconstruction of data taken with the Australian Telescope Compact Array on (top to bottom) July 17, 20, and 22, 1994. These are cuts through the dipolar magnetic equator of Jupiter (viewed from the north pole) showing the changes that occurred between the date shown and 5 days earlier. Border labels give magnetic longitudes and letters indicate the impact longitudes. The two circles are at 1 and 2 Jupiter radii. The brightness scale is the same for the three images. These images show that Jupiter's synchrotron radiation brightened considerably in localized regions after specific impacts. Reprinted from Sault *et al.* (1997a).
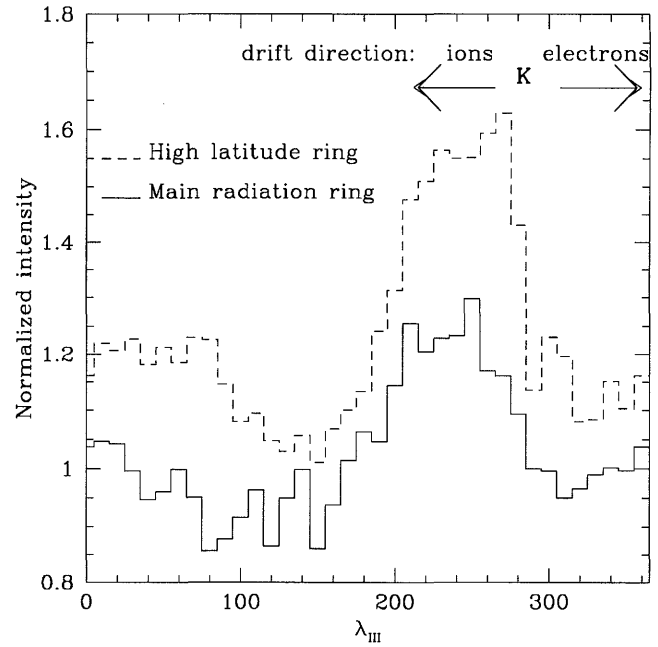
Figure 8.16. Radiation enhancement following impact K (at λ_{III} $\sim 280°$). The enhanced synchrotron radiation suggests a backward electron drift motion. Reprinted from Brecht *et al.* (2001), copyright © 2001, with permission from Elsevier.

(McGrath *et al.* 1995, Hall *et al.* 1995, Ballester *et al.* 1995). This implies negligible pickup heating by cometary materials, and that the height-integrated Pederson conductivity at the foot of the torus L shell was unaffected. As Dessler and Hill (1994) had predicted, the former basically confirms that Io is a much larger source than the fragment comae for torus mass loading. We note that the impacts took place at $L = 1.5$–2.5, so the absence of a change in ionospheric conductivity at $L = 6$ may not be surprising.

Signatures of Magnetopause Crossings

Dessler and Hill (1994) showed that the magnitude of the equilibrium potential of dust grains may increase abruptly upon crossing the magnetopause. The authors predicted that 1–1000 μm dust grains would be torn apart by electrostatic self-repulsion. Since the break-up of such grains would increase the dust surface area, this effect could be observed as a sudden brightening of the comet fragment comae. HST observations of fragment G, 3.8×10^6 km away from Jupiter (close to the magnetopause), showed a sudden brightening by a factor of ~ 3 or more, which lasted less than 20 minutes (Weaver *et al.* 1995). These were preceded 18 minutes earlier by strong Mg^+ emissions. Weaver *et al.* suggest that the brightening and Mg^+ emissions are most likely the result of dust breakup when the fragment crossed the magnetopause.

8.5.2   Explanations, Speculations, and Models

The literature contains a number of explanations for the variety of observed synchrotron phenomena, but only one detailed model. We discuss these below.

Explanations and Speculations

Soon after the first observations, Ip (1995) and de Pater *et al.* (1995) suggested that enhanced radial diffusion played an important role in the observed increase in the synchrotron emission, since the main radiation belts were seen to have shifted toward Jupiter. An increase in radial diffusion would naturally explain an increase in the synchrotron radiation, as well as a flattening of the radio spectrum. Bolton and Thorne (1995) suggested instead that pitch angle scattering might be responsible for the increase in the radio emissions. Pitch angle scattering would decrease a particle's pitch angle, lowering the altitude of its mirror point and hence putting the electron in a region of higher magnetic field strength. The higher magnetic field strength leads to an overall increase in synchrotron emission. However, the same process may also cause many particles to enter their atmospheric loss cones, reducing the number of synchrotron-emitting electrons significantly. The increased particle precipitation would enhance ionospheric IR and UV emissions. After the first impact, the radio emission decreased at the longitude of the impact site (Sault *et al.* 1997a, de Pater and Brecht 2001a).

In considering the longevity of the enhanced coherent radiation regions, Sault *et al.* (1997a) argued, based upon the data in Figure 8.15, that the brightenings built up over a 1–2 day period and stayed fixed in longitude over a period of several days. Work by de Pater *et al.* (1997b) showed that the time evolution of the enhanced radiation regions following each impact varied considerably. The only consistent feature was that the location of each enhanced radiation region was offset from the impact longitude in the ion drift direction rather than the electron drift direction. The brightened regions in the radiation belts at longitudes ~120–270° stayed coherent longer than one would expect from a straightforward application of drift theory.

Brecht *et al.* (2001) offered the explanation that the magnetic flux tubes were filled with plasma lofted by the impact. In this situation of strong plasma density inhomogeneities, normal drift motion is overwhelmed by the charge separation that would be created by the oppositely directed drifts of the ions and electrons. The charge separation leads to electric fields being created across the flux tube and subsequent current closure in the ionosphere. This process tends to bind the electrons electrically to the ions lofted by the plume into the magnetosphere. Hence, the electrons follow the ions in their slow drift around Jupiter until the strong plasma inhomogeneities are reduced.

Hill and Dessler (1999) offered some additional thoughts on the persistence of the brightened regions. They suggested that atmospheric flows created by the impacts could couple with the ionosphere and influence the electrical current system, leading to enhanced diffusion in the flux tubes of impact. Since the magnetic field strength B varies roughly as L^{-3}, the synchrotron radiation would be enhanced at the longitude of impact, a phenomenon which, according to Hill and Dessler, may last for a week, and the onset of which should be delayed by about a day after the impact. Simon and Beebe (1996) reported anticyclonic motions for a few events, with perimeter velocities up to 45 m s^{-1} in one case. These motions soon lost coherence among the regional weather patterns. The idea of a large-scale atmospheric flow coupling with the ionosphere to form coherent current systems has not been explored in detail, and merits further study.

Diffusive Shock Acceleration and Enhanced Diffusion Model

The modification of Jupiter's radiation belts was so extensive and rapid that detailed modeling was intractable, but Brecht *et al.* (2001) constructed models and theories for parts of the relevant physical processes. They merged three separate models: a diffusive shock acceleration model, a shock envelope model, and the enhanced radial diffusion model of de Pater and Brecht (2001a). Their goal was to simulate the basic shock coupling between the atmosphere, ionosphere, and magnetosphere, as discussed above.

Whether a shock propagates through the ionosphere and into the magnetosphere depends on the local Alfvén speed (see above). This turns out to be a major issue in explaining the observations. If the disturbance velocity is less than the local Alfvén speed, the upward disturbance propagates through the ionosphere as nonlinear Alfvén waves, which couple to the magnetosphere via large-amplitude electromagnetic waves and field-aligned whistlers. These affect the trapped electron distribution both through pitch angle scattering and through a sudden ~million-fold increase in the overall particle diffusion for perhaps a minute in time, as induced through scattering and an $\mathbf{E} \times \mathbf{B}$ drift, where $\mathbf{E}$ is the electric field. This process affects particles at all pitch angles, and they move toward the planet nearly instantaneously. Because the first adiabatic invariant is conserved during this process, the inward shift leads to a large localized increase in the synchrotron emission from the main radiation peaks. The high-latitude regions are only slightly affected. The change from panel (c) → (d) in Figure 8.14 shows this effect, which was observed in the early part of impact week.

Cometary impact plumes load the ionosphere with dust (some of which is charged) and increase the number of ions caught on the magnetic field lines. This lowers the local Alfvén velocity considerably. Brecht *et al.* (2001) show that after a few events the Alfvén velocity becomes low enough for shocks to form and propagate in the ionosphere. When these shocks reach the magnetosphere, they interact with particles in the radiation belts that bounce up and down field lines with small pitch angles at the L shells threading through the impact site. The direct interaction of the relativistic electrons with the shock violates all adiabatic invariants: the relativistic electrons gain energy and change their pitch angles considerably. This results in a dramatic brightening of the high-latitude regions, as exemplified in panels (c) → (e) and (d) → (f) of Figure 8.14, and as seen in the data after the K impact (Figure 8.14, panel (b)).

The interaction of the particles with electromagnetic waves and the shock induces pitch angle scattering, driving many particles into their loss cones. This explains why the observed intensity enhancement was always less than expected based upon radial diffusion theory alone. This pitch angle scattering naturally explains the ionospheric UV and X-ray emissions following the K impact. Since these emissions only appeared in the northern hemisphere, it suggests the creation of strong perturbations to the magnetic field near the impact sites caused by lofting of the ionosphere (de Pater and Brecht 2001a).
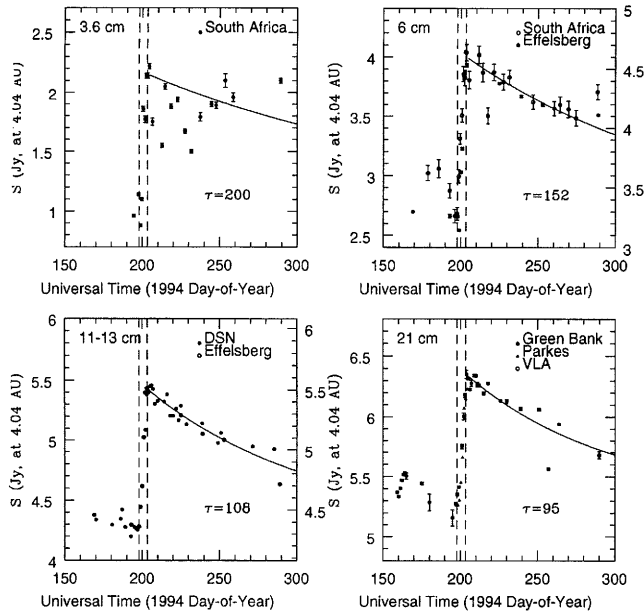
Figure 8.17. Jupiter's synchrotron radiation as a function of time. SL9 impact week is indicated by vertical dashed lines. Each panel shows a different wavelength, and symbol shapes indicate different telescopes. Superposed are curves representing an exponential fall-off with a timescale τ as indicated. Note that τ increased with decreasing wavelength and with longer data period. Adapted from Bird *et al.* (1996), Millan *et al.* (1998), Klein *et al.* (1996), and Wong *et al.* (1996).

Some impactors, regardless of size or energy, triggered substantial changes in the synchrotron emission, while others did not. Bolton and Thorne (1995) point out that impacts at $\lambda_{III} \sim 0°$–$100°$ were on L shells $\sim$2–2.5, while impacts at other longitudes were on L shells $\sim$1.5. Thus, the events at $\lambda_{III} \sim 0$–$100°$ impact L shells connected to the high latitude lobes while impacts at $\lambda_{III} \sim 120$–$250°$ occur on L shells connected to the main equatorial emission regions. The atmospheric loss cones at the longitudes of impact may also be important in calculating which impacts should lead to considerable synchrotron emission enhancements. This naturally results in maximum synchrotron enhancements at $\lambda_{III} \sim 120°$–$250°$, where the enhancements were consistently observed (de Pater and Brecht 2001a).

8.5.3   Long-Term Implications

The radio data taken during and after the impacts give unique information on diffusion processes during extreme disturbances and the recovery rate of the radiation belts. The diffusion coefficient, or cross-field transport rate, probably returned to levels within an order of magnitude of ambient by about a minute after impact (Brecht *et al.* 2001, de Pater and Brecht 2001a). The observations show that it took many months for the particle distribution to return to normal, most likely via the regular diffusion and loss processes. Figure 8.17 presents the variation in the radio intensity as a function of time for different wavelengths. The exponential decay time constant typically increased from 50–100 days in the first few months to 200–300 days when data over a full year are included. As de Pater *et al.* (1995), Bird *et al.*

(1996), and Millan *et al.* (1998) point out, the decay process is fastest at low frequencies and exceedingly slow at the higher frequencies (i.e., the spectrum continues to harden throughout the particle dissipation). Bird *et al.* and Millan *et al.* also point out that there seem to be at least two different decay processes. The first one, which operates immediately following the impacts, may be dominated by pitch angle scattering and other field-aligned processes, which are induced by the electromagnetic turbulence and whistler-mode waves triggered by the impact. The second decay process is probably the general diffusion, which over time restores the equilibrium situation, as described and modeled for Jupiter by de Pater and Goertz (1990, 1994) and others. This diffusion process is usually assumed to be independent of particle energy, but comparison of SL9 data taken at different wavelengths suggests that the general diffusion may in fact depend on a particle's energy.

8.6   CONCLUSIONS

In the chronological discussions above, several unexpected lessons emerge as the most important. These include, for example, that the reentry of the plume spreads effects 10^4 km from the impact sites in a matter of minutes, that large impacts have a dramatic effect on the magnetosphere that is driven through an ionospheric link to the atmosphere, and that impacts may be the primary source of stratospheric CO. For magnetospheric physics, SL9 provided strong evidence of the role of shocks in accelerating relativistic electrons (a phenomenon usually only seen in interplanetary shocks). It also provided evidence of huge increases in the cross-field transport rates of relativistic electrons, and it demonstrated that basic assumptions such as the charged-particle drift direction are violated in highly perturbed situations, leading to surprising results. In the atmosphere, the advection of particulates showed horizontal eddy mixing to dominate meridional transport. It also confirmed prior estimates of zonal wind decay with height.

There are still puzzles and unfinished work. The HST rings promise to teach us something, perhaps about the vertical structure of Jupiter's atmosphere and the planetary abundance of oxygen. The 2.0–2.4 μm spectra changed throughout the main event because peak shock temperatures (and therefore the chemistry in the shocks) changed. O-rich chemical models at successively higher temperatures provide the best current clues to the time-dependent appearance of the spectra. There are still substantial discrepancies between the models and the observations, however, indicating that there is still more to learn. For post-impact chemistry, the big puzzle is why SO_x did not form when other oxidized species and reduced sulfur formed in abundance. This may indicate poor mixing or inhomogeneous impactors, but other effects have not been ruled out. Further analysis and modeling of magnetospheric observations offer the possibility of learning more about the trapped radiation belts of Jupiter and possibly of Earth, such as the equilibration time of pumped belts. 3D tomographic reconstructions of all radio interferometric data would provide a more complete timeline of the magnetospheric distortions, which would better characterize the behavior of the relativistic electrons. The UV, IR, and even X-ray data may

provide insight into field-aligned processes such as precipitation and acceleration.

Since all subsequent phases depend on the impact phase, resolved, 3D impact models are a key missing requirement for a full understanding of these events. Such models should cover a horizontal extent sufficient to initialize a larger-scale model of the entry response that has much lower resolution. Those in turn should reach high enough into the plume flight phase to initialize a plume model with a grid of material velocity, density, temperature, and composition. Finally, careful tracking of the effect on the ionosphere would enable a coupled magnetosphere model. We urge modelers to publish their final plume geometries and mass–velocity distributions. Depositing time-dependent model output and the codes that generated them with the NASA Planetary Data System would enable the coupling of impact models to models of later phases. Integrating chemical models with the physical models of the plume flight and landing response phases would lead to the first realistic synthetic images of the impact sites and could solve the spectroscopy and HST rings puzzles.

Chances to observe impacts are rare on human timescales. Unlike SL9, the next event may not have multiple impacts and it may not be predicted long in advance. Contingency planning and readiness to respond quickly may thus be crucial for successful observation of the next impact. The SL9 experience underscores the need to coordinate coverage of all wavelengths and observation types continuously for one day before and several days after an impact, rather than ignoring what is thought to be obscure in order to cover multiply what one believes will be the most exciting. Many impact effects are very localized in time, space, or wavelength. Only a few observers saw important phenomena such as the McGregor and HST rings, the plumes, and the flare. Some phenomena were seen in only a subset of events and could have been missed entirely had SL9 been a single impact. It would thus be worthwhile for an international commission of interested parties (including observers, impact specialists, and telescope directors) to coordinate the assignment of observations to observatories to ensure the broadest and best observational coverage. In the end, one learns the most from the unpredicted.

REFERENCES

Ahrens, T. J., T. Takata, J. D. O'Keefe, and G. S. Orton, Impact of comet Shoemaker-Levy 9 on Jupiter, *Geophys. Res. Lett.* **21**, 1087–1090, 1994a.

Ahrens, T. J., T. Takata, J. D. O'Keefe, and G. S. Orton, Radiative signatures from impact of comet Shoemaker-Levy-9 on Jupiter, *Geophys. Res. Lett.* **21**, 1551–1553, 1994b.

Allison, M., A similarity model for the windy jovian thermocline, *Planet. Space Sci.* **48**, 753–774, 2000.

Asphaug, E. and W. Benz, Density of comet Shoemaker-Levy 9 deduced by modelling breakup of the parent rubble pile, *Nature* **370**, 120–124, 1994.

Asphaug, E. and W. Benz, Size, density, and structure of comet Shoemaker-Levy 9 inferred from the physics of tidal breakup, *Icarus* **121**, 225–248, 1996.

Ballester, G. E., W. M. Harris, G. R. Gladstone, J. T. Clarke, R. Prangé, P. D. Feldman, M. R. Combi, C. Emerich, D. F. Strobel, A. Talavera, S. A. Budzien, M. B. Vincent, T. A. Livengood, K. L. Jessup, M. A. McGrath, D. T. Hall, J. M. Ajello, L. Ben Jaffel, D. Rego, G. Fireman, L. Woodney, S. Miller, and X. Liu, Far-UV emissions from the SL9 impacts with Jupiter, *Geophys. Res. Lett.* **22**, 2425–2428, 1995.

Banfield, D., P. J. Gierasch, S. W. Squyres, P. D. Nicholson, B. J. Conrath, and K. Matthews, 2 μm spectophotometry of jovian stratospheric aerosols – scattering opacities, vertical distributions, and wind speeds, *Icarus* **121**, 389–410, 1996.

Bézard, B., Long-term response of Jupiter's thermal structure to the SL9 impacts, *Planet. Space Sci.* **45**, 1251–1270, 1997.

Bézard, B., C. A. Griffith, and D. M. Kelly, Search for NH_3 in Jupiter's stratosphere ten months after SL9's collision, *Icarus* **125**, 331–339, 1997a.

Bézard, B., C. A. Griffith, D. M. Kelly, J. H. Lacy, T. Greathouse, and G. Orton, Thermal infrared imaging spectroscopy of Shoemaker-Levy 9 impact sites: Temperature and HCN retrievals, *Icarus* **125**, 94–120, 1997b.

Bézard, B., E. Lellouch, D. Strobel, J.-P. Maillard, and P. Drossart, Carbon monoxide on Jupiter: Evidence for both internal and external sources, *Icarus* **159**, 95–111, 2002.

Bird, M. K., O. Funke, J. Neidhofer, and I. de Pater, Multifrequency radio observations of Jupiter at Effelsberg during the SL9 impact, *Icarus* **121**, 450–456, 1996.

Bjoraker, G. L., S. R. Stolovy, T. L. Herter, G. E. Gull, and B. E. Pirger, Detection of water after the collision of fragments G and K of comet Shoemaker-Levy 9 with Jupiter, *Icarus* **121**, 411–421, 1996.

Bolton, S. J., Interpretation of the observed changes in Jupiter's synchrotron radiation during and after the impacts from comet Shoemaker-Levy 9, *Planet. Space Sci.* **45**, 1359–1370, 1997.

Bolton, S. J. and R. M. Thorne, Assessment of mechanisms for jovian synchrotron variability associated with comet SL9, *Geophys. Res. Lett.* **22**, 1813–1816, 1995.

Borovička, J. and P. Spurný, Radiation study of two very bright terrestrial bolides and an application to the comet S–L 9 collision with Jupiter, *Icarus* **121**, 484–510, 1996.

Borunov, S., P. Drossart, T. Encrenaz, and V. Dorofeeva, High temperature chemistry in the fireballs formed by the impacts of comet P/Shoemaker-Levy 9 in Jupiter, *Icarus* **125**, 121–134, 1997.

Boslough, M. B., D. A. Crawford, T. G. Trucano, and A. C. Robinson, Numerical modeling of Shoemaker-Levy 9 impacts as a framework for interpreting observations, *Geophys. Res. Lett.* **22**, 1821–1824, 1995.

Boslough, M. B. E. and D. A. Crawford, Shoemaker-Levy 9 and plume-forming collisions on Earth, in *Near-Earth Objects, the United Nations International Conference*, J. L. Remo, ed., pp. 236–282, New York Academy of Sciences, 1997.

Boslough, M. B. E. and G. R. Gladstone, An impact plume model for atmospheric holes in the FUV dayglow, *Geophys. Res. Lett.* **24**, 3117–3120, 1997.

Bottke, W. F., A. Morbidelli, R. Jedicke, J. Petit, H. F. Levison, P. Michel, and T. S. Metcalfe, Debiased orbital and absolute magnitude distribution of the near-Earth objects, *Icarus* **156**, 399–433, 2002.

Brecht, S. H., M. Pesses, J. G. Lyon, N. T. Gladd, and S. W. McDonald, An explanation of synchrotron radiation

enhancement following the impact of Shoemaker-Levy 9 with Jupiter, *Geophys. Res. Lett.* **22**, 1805–1808, 1995.

Brecht, S. H., I. de Pater, D. J. Larson, and M. E. Pesses, Modification of the jovian radiation belts by Shoemaker-Levy 9: An explanation of the data, *Icarus* **151**, 25–38, 2001.

Brown, M. E., E. J. Moyer, A. H. Bouchez, and H. Spinrad, Comet Shoemaker-Levy 9: No effect on the Io plasma torus, *Geophys. Res. Lett.* **22**, 1833–1836, 1995.

Carlson, R. W., P. R. Weissman, J. Hui, M. Segura, W. D. Smythe, K. H. Baines, T. V. Johnson, P. Drossart, T. Encrenaz, F. Leader, and R. Mehlman, Some timing and spectral aspects of the G and R collision events as observed by the *Galileo* Near Infrared Mapping Spectrometer, in West and Böhnhardt (1995), pp. 69–73.

Carlson, R. W., P. Drossart, T. Encrenaz, P. R. Weissman, J. Hui, and M. Segura, Temperature, size, and energy of the Shoemaker-Levy 9 G-impact fireball, *Icarus* **128**, 251–274, 1997.

Carr, T. D., M. D. Desch, and J. K. Alexander, Phenomenology of magnetospheric radio emissions, in *Physics of the Jovian Magnetosphere*, A. J. Dessler, ed., pp. 226–284, Cambridge University Press, 1983.

Carr, T. D., F. Reyes, J. A. Phillips, J. May, L. Wang, J. Aparici, H. Alvarez, F. Olmos, L. Garcia, J. M. de Buizer, W. B. Greenman, T. Clark, J. Levy, S. Padin, and C. A. Higgins, Results of decametric monitoring of the comet collision with Jupiter, *Geophys. Res. Lett.* **22**, 1785–1788, 1995.

Chapman, C. W., *Galileo* observations of the impacts, in Noll *et al.* (1996), pp. 121–132.

Chodas, P. W. and D. K. Yeomans, The orbital motion and impact circumstances of comet Shoemaker-Levy 9, in Noll *et al.* (1996), pp. 1–30.

Clarke, J. T., R. Prangé, G. E. Ballester, J. Trauger, R. Evans, D. Rego, K. Stapelfeldt, W. Ip,. J. C. Gérard, H. Hammel, M. Ballav, L. Ben Jaffel, J. Bertaux, D. Crisp, C. Emerich, W. Harris, M. Horanyi, S. Miller, A. Storrs, and H. Weaver, HST far ultraviolet imaging of Jupiter during the impacts of comet Shoemaker-Levy-9, *Science* **267**, 1302–1307, 1995.

Cravens, T. E., Comet Shoemaker-Levy-9 impact with Jupiter: Aeronomical predictions, *Geophys. Res. Lett.* **21**, 1075–1078, 1994.

Crawford, D. A., Models of fragment penetration and fireball evolution, in Noll *et al.* (1996), pp. 133–156.

Crawford, D. A., M. B. Boslough, T. G. Trucano, and A. C. Robinson, The impact of periodic comet Shoemaker-Levy 9 on Jupiter, *Shock Waves* **4**, 47–50, 1994.

de Pater, I., The effect of comet Shoemaker-Levy 9 on Jupiter's synchrotron radiation, *Geophys. Res. Lett.* **21**, 1071–1074, 1994.

de Pater, I. and S. H. Brecht, SL9 impacts and simulations of enhanced radial diffusion, *Icarus* **151**, 39–50, 2001a.

de Pater, I. and S. H. Brecht, SL9 impacts: VLA high-resolution observations at $\lambda = 20$ cm, *Icarus* **151**, 1–24, 2001b.

de Pater, I. and C. K. Goertz, Radial diffusion models of energetic electrons and Jupiter's synchrotron radiation: I. Steady state solution, *J. Geophys. Res.* **95**, 39–50, 1990.

de Pater, I. and C. K. Goertz, Radial diffusion models of energetic electrons and Jupiter's synchrotron radiation: 2. Time variability, *J. Geophys. Res.* **99**, 2271–2287, 1994.

de Pater, I., C. Heiles, M. Wong, R. J. Maddalena, M. Bird, O. Funke, J. Neidhofer, R. M. Price, M. Kesteven, M. Calabretta, M. J. Klein, S. Gulkis, S. J. Bolton, R. S. Foster, S. Sukumar, R. G. Strom, R. S. Lepoole, T. Spoelstra, M. Robison, R. W. Hunstead, D. Campbell-Wilson, T. Ye, G. Dulk, Y. Leblanc, P. Galopeau, E. Gerard, and A. Lecacheux, The outburst of Jupiter's synchrotron radiation following the impact of comet P/Shoemaker-Levy 9, *Science* **268**, 1879–1883, 1995.

de Pater, I., M. Schulz, and S. H. Brecht, Synchrotron evidence for Amalthea's influence on Jupiter's electron radiation belt, *J. Geophys. Res.* **102**, 22 043–22 064, 1997a.

de Pater, I., F. van der Tak, R. G. Strom, and S. H. Brecht, The evolution of Jupiter's radiation belts after the impact of comet D/Shoemaker-Levy 9, *Icarus* **129**, 21–47, 1997b.

Deming, D., Prospects for jovian seismological observations following the impact of comet Shoemaker-Levy 9, *Geophys. Res. Lett.* **21**, 1095–1098, 1994.

Deming, D. and J. Harrington, Models of the Shoemaker-Levy 9 impacts: II. Radiative-hydrodynamic modeling of the plume splashback, *ApJ* **561**, 468–480, 2001.

Desch, M. D., M. L. Kaiser, W. M. Farrell, R. J. MacDowall, and R. G. Stone, Traversal of comet SL9 through the jovian magnetosphere and impact with Jupiter: Radio upper limits, *Geophys. Res. Lett.* **22**, 1781–1784, 1995.

Dessler, A. J. and T. W. Hill, Some interactions between dust from comet Shoemaker-Levy 9 and Jupiter, *Geophys. Res. Lett.* **21**, 1043–1046, 1994.

Dinelli, B. M., S. Miller, N. Achilleos, H. A. Lam, M. Cahill, J. Tennyson, M. Jagod, T. Oka, J. Hilico, and T. R. Geballe, UKIRT observations of the impact and consequences of comet Shoemaker-Levy 9 on Jupiter, *Icarus* **126**, 107–125, 1997.

Dowling, T. E., Estimate of Jupiter's deep zonal-wind profile from Shoemaker-Levy 9 data and Arnol'd's second stability criterion, *Icarus* **117**, 439–442, 1995.

Dulk, G. A., R. J. Sault, and Y. Leblanc, Jupiter's radiation belts: at the time of comet SL-9 and a year later, *Planet. Space Sci.* **45**, 1231–1236, 1997.

Encrenaz, T., P. Drossart, R. W. Carlson, and G. Bjoraker, Detection of H_2O in the splash phase of G- and R-impacts from NIMS-*Galileo*, *Planet. Space Sci.* **45**, 1189–1196, 1997.

Farrell, W. M., M. L. Kaiser, M. D. Desch, and R. J. MacDowall, Possible radio wave precursors associated with the comet Shoemaker-Levy 9/Jupiter impacts, *Geophys. Res. Lett.* **21**, 1067–1070, 1994.

Fast, K., T. Kostiuk, P. Romani, F. Espenak, T. Hewagama, A. Betz, R. Boreiko, and T. Livengood, Temporal behavior of stratospheric ammonia abundance and temperature following the SL9 impacts, *Icarus* **156**, 485–497, 2002.

Fitzsimmons, A., P. J. Andrews, R. Catchpole, J. E. Little, N. Walton, and I. P. Williams, Optical imaging of the impact plume on Jupiter from fragment L of comet d/Shoemaker-Levy 9, *MNRAS* **278**, 781–786, 1996a.

Fitzsimmons, A., P. J. Andrews, R. Catchpole, J. E. Little, N. Walton, and I. P. Williams, Reentry and ablation of cometary dust in the impact plumes of Shoemaker-Levy 9, *Nature* **379**, 801–803, 1996b.

Friedson, A. J., Formation of refractory grains in Shoemaker-Levy 9 fireballs, *Icarus* **131**, 179–197, 1998.

Friedson, A. J., R. A. West, A. K. Hronek, N. A. Larsen, and N. Dalal, Transport and mixing in Jupiter's stratosphere inferred from comet S-L9 dust migration, *Icarus* **138**, 141–156, 1999.

Galdemard, P., B. Mosser, P. O. Lagage, R. Jouan, P. Masse, and E. Pantin, 3-D analysis of the seismic response of Jupiter to the SL9 impacts: application to the CAMIRAS infrared images, *Planet. Space Sci.* **45**, 1223–1229, 1997.

Gierasch, P. J., J. A. Magalhães, and B. J. Conrath, Zonal mean properties of Jupiter's upper troposphere from *Voyager* infrared observations, *Icarus* **67**, 456–483, 1986.

Gough, D. O., Seismic consequence of the Shoemaker-Levy impact, *MNRAS* **269**, L17–L20, 1994.

Graham, J. R., I. de Pater, J. G. Jernigan, M. C. Liu, and M. E. Brown, The fragment R collision: W. M. Keck telescope observations of SL9, *Science* **267**, 1320–1323, 1995.

Griffith, C. A., B. Bezard, T. K. Greathouse, D. M. Kelly, J. H. Lacy, and K. S. Noll, Thermal infrared imaging spectroscopy

of Shoemaker-Levy 9 impact sites: Spatial and vertical distributions of NH₃, C₂H₄, and 10-μm dust emission, *Icarus* **128**, 275–293, 1997.

Guillot, T., D. Gautier, and W. B. Hubbard, NOTE: New constraints on the composition of Jupiter from *Galileo* measurements and interior models, *Icarus* **130**, 534–539, 1997.

Hall, D. T., G. R. Gladstone, F. Herbert, R. Lieu, and N. Thomas, Io torus EUV emissions during the comet Shoemaker-Levy/9 impacts, *Geophys. Res. Lett.* **22**, 3441–3444, 1995.

Hammel, H. B., R. F. Beebe, A. P. Ingersoll, G. S. Orton, J. R. Mills, A. A. Simon, P. Chodas, J. T. Clarke, E. de Jong, T. E. Dowling, J. Harrington, L. F. Huber, E. Karkoschka, C. M. Santori, A. Tiogo, D. Yeomans, and R. A. West, HST imaging of atmospheric phenomena created by the impact of comet Shoemaker-Levy 9, *Science* **267**, 1288–1296, 1995.

Harrington, J. and D. Deming, Models of the Shoemaker-Levy 9 impacts. I. Ballistic Monte Carlo plume, *ApJ* **561**, 455–467, 2001.

Harrington, J., R. P. Le Beau, K. A. Backes, and T. E. Dowling, Dynamic response of Jupiter's atmosphere to the impact of comet Shoemaker-Levy 9, *Nature* **368**, 525–527, 1994.

Herbert, F., The impact of comet Shoemaker-Levy 9 on the jovian magnetosphere, *Geophys. Res. Lett.* **21**, 1047–1050, 1994.

Herbst, T. M., D. P. Hamilton, H. Boehnhardt, and J. L. Ortiz-Moreno, SL-9 impact imaging, spectroscopy and long-term monitoring from the Calar Alto Observatory, in West and Böhnhardt (1995), pp. 119–122.

Hill, T. W., Magnetospheric effects of comet Shoemaker-Levy 9, in *Physics of Space Plasmas (1995)*, T. Chang and J. R. Jasperse, eds, pp. 205–215, MIT Center for Theoretical Geo/Cosmo Plasma Physics, 1996.

Hill, T. W. and A. J. Dessler, Midlatitude jovian aurora produced by the impact of comet Shoemaker-Levy 9, *Geophys. Res. Lett.* **22**, 1817–1820, 1995.

Hill, T. W. and A. J. Dessler, Stirring of the jovian radiation belt by comet SL-9 impacts, in *Magnetospheres of the Outer Planets Meeting*, Paris, 1999.

Hunten, D. M., W. F. Hoffmann, and A. L. Sprague, Jovian seismic waves and their detection, *Geophys. Res. Lett.* **21**, 1091–1094, 1994.

Ingersoll, A. P. and H. Kanamori, Waves from the collisions of comet Shoemaker-Levy 9 with Jupiter, *Nature* **374**, 706–708, 1995.

Ingersoll, A. P. and H. Kanamori, Waves from the Shoemaker-Levy 9 impacts, in Noll *et al.* (1996), pp. 329–345.

Ingersoll, A. P., H. Kanamori, and T. E. Dowling, Atmospheric gravity waves from the impact of comet Shoemaker-Levy 9 with Jupiter, *Geophys. Res. Lett.* **21**, 1083–1086, 1994.

Ip, W., Magnetospheric and auroral effects of the SL9 impacts, in Noll *et al.* (1996), pp. 347–373.

Ip, W.-H., Time variations of the jovian synchrotron radiation following the collisional impacts of comet Shoemaker-Levy 9-2. Flux enhancement induced by neutral atmospheric turbulence, *Planet. Space Sci.* **43**, 221–223, 1995.

Ip, W.-H. and R. Prangé, On possible magnetospheric dust interactions of comet Shoemaker-Levy 9 at Jupiter, *Geophys. Res. Lett.* **21**, 1051–1054, 1994.

Jessup, K. L., J. T. Clarke, G. E. Ballester, and H. B. Hammel, Ballistic reconstruction of HST observations of ejecta motion following Shoemaker-Levy 9 impacts into Jupiter, *Icarus* **146**, 19–42, 2000.

Kanamori, H., Excitation of jovian normal modes by an impact source, *Geophys. Res. Lett.* **20**, 2921–2924, 1993.

Kellogg, P. J., Plasma effects on the interaction of a comet with Jupiter, *Geophys. Res. Lett.* **21**, 1055–1058, 1994.

Kim, S. J., M. Ruiz, G. H. Rieke, M. J. Rieke, and K. Zahnle, High temperatures in returning ejecta from the R impact of comet SL9, *Icarus* **138**, 164–172, 1999.

Klein, M. J., S. Gulkis, and S. J. Bolton, Jupiter's synchrotron radiation: Observed variations before, during and after the impacts of comet SL-9, in *Planetary Radio Emissions IV*, H. O Rucker, S. J. Bauer, and A. Lecacheux, eds, pp. 217–224, Verlag der Österreichischen Akademie der Wissenschaften, 1996.

Knacke, R. F., S. B. Fajardo-Acosta, T. R. Geballe, and K. S. Noll, Infrared spectra of the R impact of comet Shoemaker-Levy 9, *Icarus* **125**, 340–347, 1997.

Korycansky, D. G., K. J. Zahnle, and M.-M. Mac Low, High-resolution calculations of asteroid impacts into the Venusian atmosphere, *Icarus* **146**, 387–403, 2000. Publisher's erratum: *Icarus* **147**, 592.

Korycansky, D. G., K. J. Zahnle, and M.-M. Mac Low, High-resolution simulations of the impacts of asteroids into the Venusian atmosphere: II. 3D models, *Icarus* **157**, 1–23, 2002.

Kostiuk, T., D. Buhl, F. Espenak, P. Romani, G. Bjoraker, K. Fast, T. Livengood, and D. Zipoy, Stratospheric ammonia on Jupiter after the SL9 collision, *Icarus* **121**, 431–441, 1996.

Kunde, V. G., F. M. Flasar, D. E. Jennings, B. Bézard, D. F. Strobel, B. J. Conrath, C. A. Nixon, G. L. Bjoraker, P. N. Romani, R. K. Achterberg, A. A. Simon-Miller, P. Irwin, J. C. Brasunas, J. C. Pearl, M. D. Smith, G. S. Orton, P. J. Gierasch, L. J. Spiker, R. Carlson, A. A. Mamoutkine, S. B. Calcutt, P. L. Read, F. W. Taylor, T. Fouchet, P. Parrish, A. Barucci, R. Courtin, A. Coustenis, D. Gautier, E. Lellouch, A. Marten, R. Prangé, Y. Birand, C. Ferrari, T. C. Owen, M. M. Abbas, R. E. Samuelson, F. Raulin, P. Ade, C. J. Césarsky, K. U. Grossman, and A. Coradini, Jupiter's atmospheric composition from the Cassini thermal infrared spectroscopy experiment, *Science*, Submitted, 2004.

Lagage, P. O., P. Galdemard, E. Pantin, R. Jouan, P. Masse, M. Sauvage, G. Olofsson, M. Huldtgren, L. Nordh, J. A. Belmonte, C. Regulo, J. M. Rodriguez Espinosa, L. Vidal, B. Mosser, A. Ulla, and D. Gautier, Collision of Shoemaker-Levy 9 fragments A, E, H, L, and Q1 with Jupiter: Mid-infrared light curves, *Geophys. Res. Lett.* **22**, 1773–1776, 1995.

Leblanc, Y., R. J. Sault, and G. A. Dulk, Synthesis of magnetospheric radio emissions during and after the Jupiter/SL-9 collision, *Planet. Space Sci.* **45**, 1213–1221, 1997.

Lellouch, E., Chemistry induced by the impacts: Observations, in Noll *et al.* (1996), pp. 213–242.

Lellouch, E., B. Bézard, R. Moreno, D. Bockelée-Morvan, P. Colom, J. Crovisier, M. Festou, D. Gautier, A. Marten, and G. Paubert, Carbon monoxide in Jupiter after the impact of comet Shoemaker-Levy 9, *Planet. Space Sci.* **45**, 1203–1212, 1997.

Lellouch, E., B. Bézard, J. Moses, G. Davis, P. Drossart, H. Feuchtgruber, E. Bergin, R. Moreno, and T. Encrenaz, The origin of water vapor and carbon dioxide in Jupiter's stratosphere, *Icarus* **159**, 112–131, 2002.

Levison, H. F., M. J. Duncan, K. Zahnle, M. Holman, and L. Dones, NOTE: Planetary impact rates from ecliptic comets, *Icarus* **143**, 415–420, 2000.

Limaye, S. S., Jupiter – New estimates of the mean zonal flow at the cloud level, *Icarus* **65**, 335–352, 1986.

Lognonné, P., B. Mosser, and F. A. Dahlen, Excitation of jovian seismic waves by the Shoemaker-Levy 9 cometary impact, *Icarus* **110**, 180–195, 1994.

Mac Low, M. and K. Zahnle, Explosion of comet Shoemaker-Levy 9 on entry into the jovian atmosphere, *ApJ* **434**, L33–L36, 1994.

Mac Low, M.-M., Entry and fireball models *vs.* observations: What have we learned?, in Noll *et al.* (1996), pp. 157–182.

Magalhães, J. A., A. Seiff, and R. E. Young, The stratification of Jupiter's troposphere at the *Galileo* Probe entry site, *Icarus* **158**, 410–433, 2002.

Mahaffy, P. R., H. B. Niemann, A. Alpert, S. K. Atreya, J. Demick, T. M. Donahue, D. N. Harpold, and T. C. Owen, Noble gas abundance and isotope ratios in the atmosphere of Jupiter from the *Galileo* Probe Mass Spectrometer, *J. Geophys. Res.* **105**, 15061–15072, 2000.

Marley, M. S., Seismological consequences of the collision of Shoemaker-Levy/9 with Jupiter, *ApJ* **427**, L63–L66, 1994.

McGrath, M. A., D. T. Hall, P. L. Matheson, H. A. Weaver, J. T. Trauger, T. E. Smith, N. Thomas, R. Gladstone, and N. M. Schneider, Response of the Io plasma torus to comet Shoemaker-Levy-9, *Science* **267**, 1313–1317, 1995.

McGregor, P. J., P. D. Nicholson, and M. G. Allen, CASPIR observations of the collision of comet Shoemaker-Levy 9 with Jupiter, *Icarus* **121**, 361–388, 1996.

Meadows, V. and D. Crisp, Impact plume composition from near-infrared spectroscopy, in West and Böhnhardt (1995), pp. 239–244.

Meadows, V., D. Crisp, J. Barnes, G. Orton, and J. Spencer, AAT observations of the SL9 fragment C, D, G, K, N, R, V, and W impacts with Jupiter: Lightcurves and imaging, *Icarus* **152**, 366–383, 2001.

Meadows, V. S., D. Crisp, and J. Barnes, AAT observations of the SL-9 fragment C, D, G, K, R, and W impacts with Jupiter: Spectral sequences, *Icarus*, submitted, 2004.

Melosh, H. J. and P. Schenk, Split comets and the origin of crater chains on Ganymede and Callisto, *Nature* **365**, 731–733, 1993.

Melosh, H. J., N. M. Schneider, K. J. Zahnle, and D. Latham, Ignition of global wildfires at the Cretaceous/Tertiary boundary, *Nature* **343**, 251–254, 1990.

Millan, R., D. Smits, and I. de Pater, Observations of Jupiter at 3.5 cm and 6.0 cm associated with the impact of comet P/Shoemaker-Levy 9, *Icarus* **133**, 184–191, 1998.

Miller, A., N. Achilleos, B. M. Dinelli, H. A. Lam, J. Tennyson, M.-F. Jagod, T. R. Geballe, L. M. Trafton, R. D. Joseph, G. E. Ballester, K. Baines, T. Y. Brooke, and G. Orton, The effect of the impact of comet Shoemaker-Levy 9 on Jupiter's aurorae, *Geophys. Res. Lett.* **22**, 1629–1632, 1995.

Molina, A., F. Moreno, and O. Munoz, Aerosol debris in the core and crescent-shaped regions of comet P/Shoemaker-Levy 9 H and G fragment impact sites on Jupiter, *Icarus* **127**, 213–220, 1997.

Moreno, R., A. Marten, Y. Biraud, B. Bézard, E. Lellouch, G. Paubert, and W. Wild, Jovian stratospheric temperature during the two months following the impacts of comet Shoemaker-Levy 9, *Planet. Space Sci.* **49**, 473–486, 2001.

Moses, J. I., SL9 impact chemistry: Long-term photochemical evolution, in Noll *et al.* (1996), pp. 243–268.

Moses, J. I., Dust ablation during the Shoemaker-Levy 9 impacts, *J. Geophys. Res.* **102**, 21619–21644, 1997.

Nakano, S., T. Kobayashi, E. Meyer, E. Obermair, H. Raab, Z. Sekanina, and B. G. Marsden, Periodic comet Shoemaker-Levy 9 (1993e), *IAU Circ.* **5800**, 1, 1993.

Nicholson, P. D., Earth-based observations of impact phenomena, in Noll *et al.* (1996), pp. 81–109.

Nicholson, P. D., P. J. Gierasch, T. L. Hayward, C. A. McGhee, J. E. Moersch, S. W. Squyres, J. Van Cleve, K. Matthews, G. Neugebauer, D. Shupe, A. Weinberger, J. W. Miles, and B. J. Conrath, Palomar observations of the R impact of comet Shoemaker-Levy 9: II. Spectra, *Geophys. Res. Lett.* **22**, 1617–1620, 1995a.

Nicholson, P. D., P. J. Gierasch, T. L. Hayward, C. A. McGhee, J. E. Moersch, S. W. Squyres, J. Van Cleve, K. Matthews, G. Neugebauer, D. Shupe, A. Weinberger, J. W. Miles, and B. J. Conrath, Palomar observations of the R impact of comet Shoemaker-Levy 9: I. Light curves, *Geophys. Res. Lett.* **22**, 1613–1616, 1995b.

Niemann, H. B., S. K. Atreya, G. R. Carignan, T. M. Donahue, J. A. Haberman, D. N. Harpold, R. E. Hartle, D. M. Hunten,

W. T. Kasprzak, P. R. Mahaffy, T. C. Owen, and S. H. Way, The composition of the jovian atmosphere as determined by the *Galileo* Probe Mass Spectrometer, *J. Geophys. Res.* **103**, 22831–22846, 1998.

Noll, K. S., M. A. McGrath, L. M. Trafton, S. K. Atreya, J. J. Coldwell, H. A. Weaver, R. V. Yelle, C. Barnet, and S. Edgington, HST spectroscopic observations of Jupiter after the collision of comet Shoemaker-Levy 9, *Science* **267**, 1307–1313, 1995.

Noll, K. S., H. A. Weaver, and P. D. Feldman, eds, *The Collision of Comet Shoemaker-Levy 9 and Jupiter, IAU Colloquium 156*, Cambridge University Press, 1996.

Ortiz, J. L., G. Orton, F. Moreno, A. Molina, S. Larson, and P. Yanamandra-Fisher, The Shoemaker-Levy 9 H impact: Some results from the William Herschel Telescope, *A&A* **324**, 357–365, 1997.

Orton, G., M. A'Hearn, K. Baines, D. Deming, T. Dowling, J. Goguen, C. Griffith, H. Hammel, W. Hoffmann, D. Hunten, D. Jewitt, T. Kostiuk, S. Miller, K. Noll, K. Zahnle, N. Achilleos, A. Dayal, L. Deutsch, F. Espenak, P. Esterle, J. Friedson, K. Fast, J. Harrington, J. Hora, R. Joseph, D. Kelly, R. Knacke, J. Lacy, C. Lisse, J. Rayner, A. Sprague, M. Shure, K. Wells, P. Yanamandra-Fisher, D. Zipoy, G. Bjoraker, D. Buhl, W. Golisch, D. Griep, C. Kaminski, C. Arden, A. Chaikin, J. Goldstein, D. Gilmore, G. Fazio, T. Kanamori, H. Lam, T. Livengood, M.-M. MacLow, M. Marley, T. Momary, D. Robertson, P. Romani, J. Spitale, M. Sykes, J. Tennyson, D. Wellnitz, and S.-W. Ying, Collision of comet Shoemaker-Levy 9 with Jupiter observed by the NASA Infrared Telescope Facility, *Science* **267**, 1277–1282, 1995.

Owen, T., P. Mahaffy, H. B. Niemann, S. Atreya, T. Donahue, A. Bar-Nun, and I. de Pater, A low-temperature origin for the planetesimals that formed Jupiter, *Nature* **402**, 269–270, 1999.

Pankine, A. A. and A. P. Ingersoll, Ejecta pattern of the impact of comet Shoemaker-Levy 9, *Icarus* **138**, 157–163, 1999.

Prangé, R., I. M. Engle, J. T. Clarke, M. Dunlop, G. E. Ballester, W. H. Ip, S. Maurice, and J. Trauger, Auroral signature of comet Shoemaker-Levy-9 in the jovian magnetosphere, *Science* **267**, 1317–1320, 1995.

Pryor, W. R., C. Y. Na, A. L. Cochran, W. D. Cochran, E. S. Barker, B. J. Armosky, and C. E. Pulliam, McDonald Observatory data on the comet Shoemaker-Levy 9 impacts on Jupiter and the resulting haze particles, *Planet. Space Sci.* **45**, 1299–1313, 1997.

Roos-Serote, M., A. Barucci, J. Crovisier, P. Drossart, M. Fulchignoni, J. Lecacheux, and F. Roques, Metallic emission lines during the impacts L and Q1 of comet Shoemaker-Levy 9 in Jupiter, *Geophys. Res. Lett.* **22**, 1621–1624, 1995.

Roulston, M. S. and T. J. Ahrens, Impact mechanics and frequency of SL9-type events on Jupiter, *Icarus* **126**, 138–147, 1997.

Sanchez-Lavega, A., J. M. Gomez, J. F. Rojas, J. R. Acarreta, J. Lecacheux, F. Colas, R. Hueso, and J. Arregui, Long-term evolution of comet SL-9 impact features: July 1994–September 1996, *Icarus* **131**, 341–357, 1998.

Sault, R. J., Y. Leblanc, and G. A. Dulk, Localized brightenings in Jupiter's radiation belts resulting from comet SL9 impacts, *Geophys. Res. Lett.* **24**, 2395–2398, 1997a.

Sault, R. J., T. Oosterloo, G. A. Dulk, and Y. Leblanc, The first three-dimensional reconstruction of a celestial object at radio wavelengths: Jupiter's radiation belts, *A&A* **324**, 1190–1196, 1997b.

Schleicher, H., H. Balthasar, M. Knolker, W. Schmidt, and K. Jockers, The impact of fragment 'L' of comet SL-9 on Jupiter, *Earth, Moon, and Planets* **66**, 13–17, 1994.

Schulz, R., T. Encrenaz, J. A. Stüwe, and G. Wiedemann, Near-IR emissions in the upper jovian atmosphere after SL9 impact: Indications of possible northern counterparts, *Geophys. Res. Lett.* **22**, 2421–2424, 1995.

Scotti, J. V. and H. J. Melosh, Estimate of the size of comet Shoemaker-Levy 9 from a tidal breakup model, *Nature* **365**, 733–735, 1993.

Shoemaker, C. S., E. M. Shoemaker, D. H. Levy, J. V. Scotti, P. Bendjoya, and J. Mueller, Comet Shoemaker-Levy (1993e), *IAU Circ.* **5725**, 1, 1993.

Shoemaker, E. M., P. J. Hassig, and D. J. Roddy, Numerical simulations of the Shoemaker-Levy 9 impact plumes and clouds: A progress report, *Geophys. Res. Lett.* **22**, 1825–1828, 1995.

Shuvalov, V. V., Atmospheric plumes created by meteoroids impacting the Earth, *J. Geophys. Res.* **104**, 5877–5890, 1999.

Simon, A. A. and R. F. Beebe, Jovian tropospheric features – Wind field, morphology, and motion of long-lived systems, *Icarus* **121**, 319–330, 1996.

Solem, J. C., Density and size of comet Shoemaker-Levy 9 deduced from a tidal breakup model, *Nature* **370**, 349–351, 1994.

Solem, J. C., Cometary breakup calculations based on a gravitationally-bound agglomeration model: The density and size of Shoemaker-Levy 9, *A&A* **302**, 596–608, 1995.

Sprague, A. L., G. L. Bjoraker, D. M. Hunten, F. C. Witteborn, R. W. H. Kozlowski, and D. H. Wooden, Water brought into Jupiter's atmosphere by fragments R and W of comet SL-9, *Icarus* **121**, 30–37, 1996.

Takata, T. and T. J. Ahrens, Impact of comet Shoemaker-Levy 9-size, origin, and plumes: Comparison of numerical analysis with observations, *Icarus* **125**, 317–330, 1997.

Takata, T., J. D. O'Keefe, T. J. Ahrens, and G. S. Orton, comet Shoemaker-Levy 9: Impact on Jupiter and plume evolution, *Icarus* **109**, 3–19, 1994.

Waite, J. H., G. R. Gladstone, K. Franke, W. S. Lewis, A. C. Fabian, W. N. Brandt, C. Na, F. Haberl, J. T. Clarke, K. C. Hurley, M. Sommer, and S. Bolton, ROSAT observations of X-ray emissions from Jupiter during the impact of comet Shoemaker-Levy 9, *Science* **268**, 1598–1601, 1995.

Walter, C. M., M. S. Marley, D. M. Hunten, A. L. Sprague, W. K. Wells, A. Dayal, W. F. Hoffmann, M. V. Sykes, L. K. Deutsch, G. G. Fazio, and J. L. Hora, A search for seismic waves from the impact of the SL/9 R fragment, *Icarus* **121**, 341–350, 1996.

Walterscheid, R. L., D. G. Brinkman, and G. Schubert, Wave disturbances from the comet SL-9 impacts into Jupiter's atmosphere, *Icarus* **145**, 140–146, 2000.

Weaver, H. A., M. F. A'Hearn, C. Arpigny, D. C. Boice, P. D Feldman, S. M. Larson, P. Lamy, D. H. Levy, B. G. Marsden, K. J. Meech, K. S. Noll, J. V. Scotti, Z. Sekanina, C. S Shoemaker, E. M. Shoemaker, T. E. Smith, S. A. Stern, A. D Storrs, T. Trauger, D. K. Yeomans, and B. Zellner, The Hubble Space Telescope (HST) observing campaign on comet Shoemaker-Levy 9, *Science* **267**, 1282–1288, 1995.

West, R. A., Particulate matter in Jupiter's atmosphere from the impacts of comet P/Shoemaker-Levy 9, in Noll *et al.* (1996) pp. 269–292.

West, R. A., E. Karkoschka, A. J. Friedson, M. Seymour K. H. Baines, and H. B. Hammel, Impact debris particles in Jupiter's stratosphere, *Science* **267**, 1296–1301, 1995.

West, R. M., Nature and structure of the impacting objects, in West and Böhnhardt (1995), pp. 407–410.

West, R. M. and H. Böhnhardt, eds., *Proceedings of the European Shoemaker-Levy 9 Conference, held 13–15 February 1995*, no. 52 in ESO Conference and Workshop Proceedings, European Southern Observatory, 1995.

Wilson, P. D. and C. Sagan, Nature and source of organic matter in the Shoemaker-Levy 9 jovian impact blemishes, *Icarus* **129**, 207–216, 1997.

Wong, M. H., I. de Pater, C. Heiles, R. Millan, R. J. Maddalena, M. Kesteven, R. M. Price, and M. Calabretta, Observations of Jupiter's 20-cm synchrotron emission during the impacts of comet P/Shoemaker-Levy 9, *Icarus* **121**, 457–468, 1996.

Yelle, R. V. and M. A. McGrath, Ultraviolet spectroscopy of the SL9 impact sites, *Icarus* **119**, 90–111, 1996.

Zahnle, K., Dynamics and chemistry of SL9 plumes, in Noll *et al.* (1996), pp. 183–212.

Zahnle, K. and M.-M. Mac Low, The collision of Jupiter and comet Shoemaker-Levy 9, *Icarus* **108**, 1–17, 1994.

Zahnle, K. and M.-M. Mac Low, A simple model for the light curve generated by a Shoemaker-Levy 9 impact, *J. Geophys. Res.* **100**, 16 885–16 894, 1995.

Zahnle, K., M.-M. Mac Low, K. Lodders, and B. Fegley, Sulfur chemistry in the wake of comet Shoemaker-Levy 9, *Geophys. Res. Lett.* **22**, 1593–1596, 1995.

Zahnle, K. J., P. Schenk, H. Levison, and L. Dones, Cratering rates in the outer solar system, *Icarus*, **163**, 263–289, 2003.

Zarka, P., The auroral radio emissions from planetary magnetospheres – What do we know, what don't we know, what do we learn from them?, *Advances in Space Research* **12**, 99–115, 1992.

Zel'dovich, Y. B. and Y. P. Raizer, *Physics of Shock Waves and High-Temperature Hydrodynamic Phenomena*, Academic Press, 1967.